

Rethinking Whole-Body CT Image Interpretation: An Abnormality-Centric Approach

Ziheng Zhao^{1,2*}, Lisong Dai^{3*}, Ya Zhang^{1,2}, Yanfeng Wang^{1,2†}, Weidi Xie^{1,2†}

¹School of Artificial Intelligence, Shanghai Jiao Tong University

²Shanghai Artificial Intelligence Laboratory

³Department of Radiology, Renmin Hospital of Wuhan University

<https://github.com/zhaoziheng/OminiAbnorm-CT>

Abstract

Automated interpretation of CT images—particularly localizing and describing abnormal findings across multi-plane and whole-body scans—remains a significant challenge in clinical radiology. This work aims to address this challenge through four key contributions: (i) On taxonomy, we collaborate with senior radiologists to propose a comprehensive hierarchical classification system, with 404 representative abnormal findings across all body regions; (ii) On data, we contribute a dataset containing over 14.5K CT images from multiple planes and all human body regions, and meticulously provide grounding annotations for over 19K abnormalities, each linked to the detailed description and cast into the taxonomy; (iii) On model development, we propose **OminiAbnorm-CT**, which can automatically ground and describe abnormal findings on multi-plane and whole-body CT images based on text queries, while also allowing flexible interaction through visual prompts; (iv) On benchmarks, we establish three representative evaluation tasks based on real clinical scenarios. Through extensive experiments, we show that OminiAbnorm-CT can significantly outperform existing methods on all the tasks and metrics.

1 Introduction

Computed Tomography (CT) imaging has become a cornerstone of modern medicine, with over 3 billion scans performed annually around the world. The interpretation of these scans—particularly the generation of radiology reports—plays a crucial role in guiding clinical decision-making. However, systematically identifying and characterizing abnormal findings in whole-body CT images remains a cognitively demanding and time-consuming task for radiologists [48].

In the recent literature, artificial intelligence has started to make significant progress in CT image interpretation, particularly along two directions: *first*, AI models have been developed for organ-level segmentation [52, 28], that enable precise anatomical labeling and organ-grounded report generation [60, 12]. Yet a critical gap remains: segmenting organs alone is insufficient for clinical utility. What ultimately matters to clinicians are abnormal findings—lesions and any anomalies that inform diagnosis and treatment; *second*, models for automatic report generation have been trained on the recently introduced datasets with paired CT scans and corresponding radiology reports, describing clinical findings and impressions [10, 19]. However, these datasets are typically limited to specific anatomical regions—most commonly chest CT—and often lack explicit visual grounding, which reduces explainability and increases the risk of hallucinated content. To address the above-mentioned

*Equal contributions

†Corresponding author

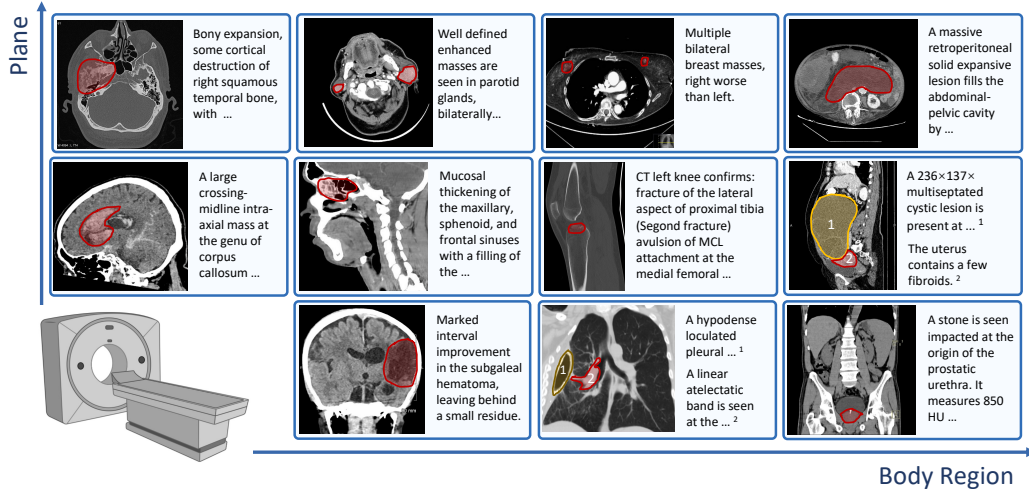


Figure 1: **OminiAbnorm-CT-14K** is the first large-scale dataset for abnormal findings grounding and description across multi-plane and whole-body CT images. It covers 349 representative abnormal findings from 82 anatomical structures and 40 major systems or organs.

challenges, we aim to explore the potential to develop a system that automatically **detects, localizes, and describes all abnormal findings across multi-plane, whole-body CT images**. This paradigm shift moves beyond regional reporting and anatomical segmentation, aligning AI interpretation more closely with the practical demands of radiological diagnosis.

One crucial barrier to developing such a system is the absence of a unified, clinically meaningful taxonomy of abnormalities, which presents a major challenge for defining task scope and establishing continuous benchmarks. In this paper, we collaborated with 7 radiologists from 3 centers (each with 10-16 years of experience) to construct a detailed hierarchical taxonomy covering 404 representative abnormal findings, that are organized across 40 major anatomical regions and 82 sub-regions.

Building on this foundation, we introduce **OminiAbnorm-CT-14K**—the first large-scale dataset designed for abnormality grounding and description on multi-plane whole-body CT imaging. It comprises 14.5K CT images from Radiopaedia [1], covering axial, coronal, and sagittal planes and diverse anatomical regions. All images and the paired reports have been rigorously reviewed by experienced radiologists. We invite 4 radiologists (with at least 7 years’ experience) to manually annotate around 19K abnormal findings on the images in the format of either bounding box or segmentation masks. All regional annotations are linked to the corresponding report descriptions, and further cast into our proposed taxonomy. These annotations cover 349 out of the 404 representative abnormal findings (86%) defined in our taxonomy across whole-body CT images. This dataset addresses a critical gap in the field, by providing high-quality, clinically relevant annotations at scale—overcoming limitations in existing datasets caused by privacy constraints and the high cost of expert annotation. All our annotations will be released to the community, while the images are accessible for research purposes after applying and paying the required fee to Radiopaedia³.

Leveraging OminiAbnorm-CT-14K, we develop **OminiAbnorm-CT**, a novel system for grounded CT image interpretation. By bridging a multi-modal language model with a specialized segmentation module in a bidirectional workflow, it enables dynamic invocation of the segmentation module during the text generation, and grounded abnormality interpretation based on the segmentation results. In contrast to prior approaches—which often lack grounding abilities, generalizability across planes and body regions, or flexibility in prompt handling—OminiAbnorm-CT enables automatic localization and description of abnormalities across multi-plane, whole-body CT scans. More importantly, OminiAbnorm-CT is designed to robustly interpret diverse textual references and visual prompts, enabling interactive and clinically adaptive use cases aligned with radiologists’ workflows.

For a comprehensive evaluation, we define three clinically relevant tasks: (i) grounded report generation, (ii) text-guided grounded report generation, and (iii) visual-prompted report generation.

³<https://radiopaedia.org/licence#data-sets>

Experiment results show that OminiAbnorm-CT significantly outperforms existing baselines across all tasks, marking a substantial step toward explainable, abnormality-centric CT imaging interpretation.

In summary, our contributions to advance abnormality-centric grounded CT image interpretation can be summarized as: (i) We propose a comprehensive taxonomy for abnormalities on CT images, presented in Section 2; (ii) We build **OminiAbnorm-CT-14K**, the first dataset for abnormality grounding and description across multi-plane whole-body CT images, detailed in Section 3; (iii) We develop a novel system **OminiAbnorm-CT**, for automatically localizing and reporting abnormalities, illustrated in detail in Section 4; (iv) We set up a comprehensive benchmark with three clinically representative tasks, and demonstrate the superiority of OminiAbnorm-CT in Section 5.

2 Taxonomy for Abnormal Findings

Given the diversity of abnormal findings, their complex relationships and synonyms, we first construct a comprehensive taxonomy system, to categorize all the abnormalities into representative classes.

Our taxonomy is guided by four fundamental principles to ensure scientific rigor, systematic organization, and clinical utility: (i) **comprehensive coverage**. It should include all the clinically significant abnormalities, encompassing both lesions and the abnormal changes on anatomical structures; (ii) **image-based definition**. Each abnormal finding is precisely characterized by its observable features on the radiology scan, such as physical properties and morphological characteristics, that form the essential foundation for diagnosis; (iii) **hierarchical organization**. Findings are grouped by clinically important anatomical structures and major systems or organs, aligning with standard image interpretation protocols. While cross-regional structures (like skeletal systems) remain independent groups for conciseness; (iv) **modular design**. Each category represents a fundamental, independent finding that can be combined with others to express complex and multifaceted abnormalities.

The taxonomy is developed through the following three stages, involving 7 radiologists with 10 to 16 years of experience from three clinical centers, (i) we establish an anatomical hierarchy framework based on standard atlases and classic textbooks for human anatomy [17]; (ii) the radiologists then systematically catalog the abnormal findings under each anatomical structure, based on their clinical experience and several authoritative textbooks [2, 18, 41] on medical imaging and radiological pathology; lastly, (iii) the radiologists conduct rigorous cross-validation and discussion to establish precise consensus on the definitions of controversial or ambiguous abnormalities.

We finally identified 404 representative abnormalities across 82 anatomies throughout the human body, organized within 40 major organs and systems. The details can be found in Appendix Section A.11.

3 Dataset Curation

In this section, we present OminiAbnorm-CT-14K, which establishes a data foundation for abnormality grounding and interpretation across whole-body CT images. The dataset construction pipeline is illustrated in Figure 2. Here, we start with an overview of the limitations of existing datasets in Section 3.1, which motivate the dataset construction. We then describe the data source in Section 3.2, detail the annotation procedure in Section 3.3, outline the extension to instruction-style data in Section 3.4, and conclude with a summary in Section 3.5.

3.1 Limitation in Existing Datasets

We analyze several widely used public datasets relevant to our task (summarized in Appendix Table 6) and identify the following limitations: (i) **limited annotation coverage**. Most datasets provide grounding annotations for only a small subset of lesion types. Despite efforts to map existing labels to our proposed taxonomy, the majority of abnormal finding categories remain unannotated; (ii) **restricted imaging scope**. Existing datasets are primarily limited to axial-plane CT images or focus on specific anatomical regions, overlooking the growing clinical need for interpretation across multi-plane, whole-body CT scans; (iii) **insufficient image-report alignment**. Many datasets lack explicit associations between localized abnormalities in the images and their corresponding descriptions in radiology reports, hindering the development of grounded, explainable systems. These limitations make existing datasets inadequate for benchmarking or developing models capable of automatic detection, localization, and description of abnormal findings in multi-plane, whole-body CT imaging.

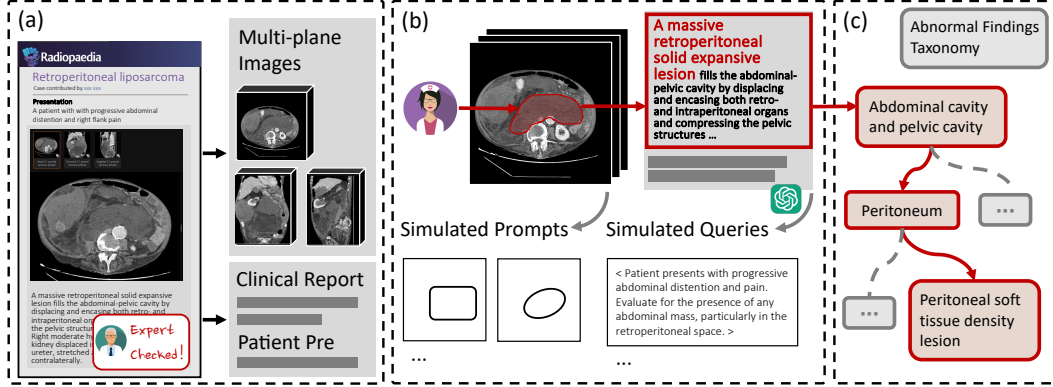


Figure 2: **Data curation overview.** (a) The CT image-report pairs are collected from an open-sourced and expert-checked website; (b) and (c) Radiologists provide grounding annotation on any abnormal findings, link to their text description in reports, and categorize into the taxonomy devised by a group of senior radiologists. The annotated data are further extended to instruction data with simulated visual prompts and text queries.

3.2 Data Source

Following prior works [53, 64, 54], we collect raw data from Radiopaedia [1], a publicly accessible platform of peer-reviewed clinical cases contributed by clinicians worldwide, with appropriate privacy safeguards. After application, we have obtained proper permission for all data used in this study. Shown in Figure 2(a), each case includes radiology scans across various planes and anatomical regions, along with patient background information and detailed clinical reports describing findings and diagnoses. In total, we collected 46,721 CT images paired with 14,920 clinical reports.

3.3 Annotation Pipeline

As illustrated in Figure 2(b) and (c), our goal is to produce grounding annotations for all abnormal findings in the collected CT images, *i.e.*, linking them to corresponding textual descriptions in clinical reports, and categorizing them using our proposed taxonomy. To reduce annotation burden, we adopt a two pre-processing strategy: (i) **image-side pre-processing**. Rather than annotating entire scans, we focus on the key slice and its 8 adjacent slices, as identified and verified by radiologists to be the most informative and representative; (ii) **text-side pre-processing**. We employ GPT-4o [25] to extract findings from the reports and identify abnormalities using RaTEScore [62].

Here, we recruited 4 clinicians with at least 7 years of radiology experience as annotators. To ensure high-quality annotations, we followed three core principles: (i) **representative slices**. Select the most representative slice(s) for annotation when abnormalities are present; (ii) **complete annotation**. Annotate all abnormal findings visible on selected slices; (iii) **vision-language consistency**. Only annotate abnormalities identifiable in provided slices; similarly, linked descriptions must reflect findings visible in these slices. For example, when a report mentions organ enlargement, the finding should not be annotated if enlargement cannot be confidently determined from the available slices.

Throughout the annotation process, we continuously refined OminiAbnorm-CT-14K based on annotator feedback: (i) **taxonomy refinement**. We remove or merge 4 less representative categories, add 22 previously omitted but clinically important ones, and revise 21 categories for improved clarity and expression; (ii) **long-tail mitigation**. To address data imbalance, we identify the underrepresented categories and use GPT-4o to filter scans referencing these rare findings, prioritizing them for annotation. As shown in Appendix Section A.6, it has significantly mitigated the long-tail distribution.

3.4 Extension to Instruction Data

As shown in Figure 2(b), we extend our annotated data to support three instruction tasks that simulate realistic clinical scenarios: (i) **grounded report generation** simulates a comprehensive examination. We format instructions to detect, ground, and describe all abnormal findings on CT images; (ii) **text-guided grounded report generation** involves responding to text queries about

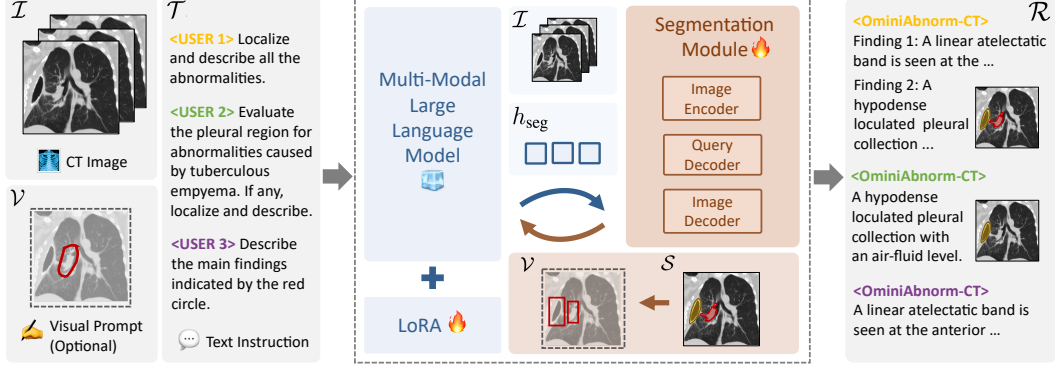


Figure 3: **OminiAbnorm-CT**. We bridge a multi-modal language model and a segmentation module, to allow grounding evidence acquisition during the generation of abnormality description, and further enhance its comprehension for flexible usage with text instruction and visual prompts.

specific abnormalities of interest. For instance, for a patient with tuberculous empyema history, checking any abnormality related to it. We generate these queries using GPT-4o based on clinical reports, patient presentations, and medical history, simulating how radiologists approach images with prior knowledge; (iii) **visual prompted report generation** focuses on interpreting the marked abnormality. We create visual prompts from annotation masks using various formats, *e.g.*, bounding box, ellipse, contour, and cropped region. This simulates a semi-automated workflow where the model elaborates the clinician-identified abnormality in details. More details are in Appendix Section A.10.

3.5 Summary

We prioritize axial CT images for annotation, while also incorporating coronal and sagittal images based on clinical recommendations. In total, we annotated 18,969 abnormalities on 9,990 axial scans, 2,738 coronal scans, and 1,803 sagittal scans. Representative examples are shown in Figure 1, and the distribution of annotated abnormalities is detailed in Appendix Section A.11. Annotation quality is verified by a senior radiologist with 12 years’ experience, with details in Appendix A.5.

4 OminiAbnorm-CT

This section presents the details of OminiAbnorm-CT, a novel system for grounded CT image interpretation. We start with the problem formulation in Section 4.1, then its architectural details in Section 4.2 and finally the training details in Section 4.3.

4.1 Problem Formulation

Given a CT image ($\mathcal{I} \in \mathbb{R}^{H \times W \times D}$), this paper aims to build a model $\Phi_\theta(\cdot)$, that enables generating the textual descriptions for abnormal regions, with intermediate groundings when necessary:

$$\{\mathcal{R}, \mathcal{S}\} = \Phi_\theta(\mathcal{T}, \mathcal{I}, \mathcal{V}), \quad (1)$$

where \mathcal{T} is the text instruction, $\mathcal{V} \in \mathbb{R}^{H \times W}$ (optional) is the visual prompt on a key slice from the users, for example, bounding boxes, ellipse, contour. \mathcal{R} denotes the generated description for abnormalities, and $\mathcal{S} \in \mathbb{R}^{H \times W}$ refers to the (optional) grounding results on the key slice.

In contrast to the conventional approaches, $\Phi_\theta(\cdot)$ can interpret user-provided textual queries and ground arbitrary abnormal findings across multi-plane CT images spanning the entire human body, and generate corresponding descriptions. Additionally, it also supports visual prompts that allow the model to elaborate on user-highlighted abnormalities, enabling an interactive workflow where users can iteratively refine or correct the grounding results for more precise and context-aware descriptions.

4.2 Architecture

The overall architecture of OminiAbnorm-CT is illustrated in Figure 3, which comprises a standard multi-modal language model and a segmentation module. Our core innovation lies in the integration

of them, which enables localizing the abnormality and generating a textual description (findings), supporting flexible interaction through both visual prompts and textual instructions.

Multi-modal language model functions as the core to comprehend user instruction, invoke the segmentation module properly, and document the abnormal findings based on the grounding evidence. Specifically, in one workflow to generate grounded reports, given a CT image (\mathcal{I}) and text instruction (\mathcal{T}) as user input, it will first reason for the specific abnormal findings of interest for the user (or simply any abnormalities). For instance, when referring to patient history of tuberculous empyema, it should focus on related abnormalities including pleural thickening, calcifications, etc.

Then, to let it acquire grounding evidence, we expand the vocabulary with special token <SEG> as grounding request, which will invoke the segmentation module during generation. We extract its hidden state h_{seg} from the last decoder layer as the prompt for the segmentation module, which encapsulates the targeted abnormal findings:

$$\mathcal{S} = \Phi_{\text{seg}}(\mathcal{I}, h_{\text{seg}}), h_{\text{seg}} \in \mathbb{R}^d \quad (2)$$

Given the segmentation results (\mathcal{S}), we convert it to visual prompt (\mathcal{V}) in box format, *i.e.*, directly overlay it on the original image to create a new input image (\mathcal{I}'), and the multi-modal language model could seamlessly continue generating the abnormality description (\mathcal{R}) based on it:

$$\mathcal{R} = \Phi_{\text{MLLM}}(\mathcal{T}, \mathcal{I}'), \mathcal{I}' = \mathcal{I} \oplus \mathcal{V} \quad (3)$$

where \oplus represents the superimposing operation. This leverages the inherent ability of multi-modal language model to perceive visual markers [8], guiding its attention to specific regions of interest.

Note that, the above design naturally supports another workflow when users have manually delineated specific abnormalities, or intend to refine the grounding results. In such case, \mathcal{V} can also be user-input visual prompts on the image, and the multi-modal language model elaborates the user-highlighted abnormality following Equation 3.

Segmentation module is invoked for abnormality grounding based on the CT image (\mathcal{I}) and prompt (h_{seg}), summarized as Equation 2. Specifically, it first adopts an encoder-decoder backbone to derive image features:

$$(v, u) = \Phi_{\text{seg}}(\mathcal{I}), v \in \mathbb{R}^{H' \times W' \times d'}, u \in \mathbb{R}^{H \times W \times d}, \quad (4)$$

where v denotes concatenation of multi-scale image embeddings along the channel dimension, which are down-sampled from each encoder layer to a unified resolution, and u is the pixel-level dense feature from the last decoder layer. To bridge the gap between latent spaces, we further align the segmentation prompt (h_{seg}) with the image embeddings (v):

$$q = \Phi_{\text{crossattn}}(v, f(h_{\text{seg}})), q \in \mathbb{R}^d \quad (5)$$

where f is a projection layer for dimension consistency, and $\Phi_{\text{crossattn}}$ is a cross-attention module treating v as key and value, $f(h_{\text{seg}})$ as query. The segmentation prediction is then derived by performing dot product between the adapted feature q and u :

$$\mathcal{S} = q \cdot u, \mathcal{S} \in \mathbb{R}^{H \times W}, \quad (6)$$

4.3 Training

Training object. We train the multi-modal language model and the segmentation module jointly with a text generation loss and a segmentation loss:

$$\mathcal{L}_{\text{txt}} = \text{CE}(\hat{\mathcal{R}}, \mathcal{R}), \mathcal{L}_{\text{seg}} = \text{BCE}(\hat{\mathcal{S}}, \mathcal{S}) + \text{DICE}(\hat{\mathcal{S}}, \mathcal{S}) \quad (7)$$

Training data. Our training data primarily originates from OminiAbnorm-CT-14K, and is formulated into three instruction data formats as illustrated in Section 3.4. Additionally, we incorporate two types of data as supplements: (i) **lesion segmentation data**. This type of data can be formulated into grounding tasks and utilized to enhance the grounding ability. A detailed list of these datasets can be found in Appendix Table 6; (ii) **medical VQA data**. This type of data is involved to maintain our model’s generalization capabilities with more diverse question types. Specifically, we take CT images and corresponding question-answering data from PubMedVision [9].

Table 1: **Quantitative results on visual prompted report generation.** Results are averaged within each category and then across all categories, with the best **bolded** and the second best underlined. Models optimized with medical data are marked with ✓.

Model	B-1	B-2	B-3	RTSc	BTSc	MTR	R-1	R-L	RG
<i>Axial (n=2193)</i>									
GPT-4o	<u>15.80</u>	<u>6.15</u>	<u>1.59</u>	39.04	84.58	<u>19.31</u>	<u>18.62</u>	14.41	<u>6.51</u>
QWen2.5-VL-7B	11.57	4.20	0.76	38.35	84.10	16.68	14.26	11.09	3.85
ViP-LLaVA	15.21	4.49	0.69	33.07	<u>85.15</u>	13.65	17.41	<u>14.68</u>	3.35
MedFlamingo ✓	11.26	1.71	0.00	17.35	80.34	9.43	11.69	10.55	0.50
MedDr ✓	9.54	2.46	0.41	32.24	78.80	9.13	12.23	10.34	3.74
LLaVA-Med ✓	15.55	4.23	0.55	39.08	84.68	15.58	17.67	13.55	6.06
BiomedGPT ✓	10.80	4.16	0.71	38.16	83.19	15.77	13.40	10.81	4.65
OminiAbnorm-CT ✓	18.03	6.65	1.80	42.81	86.35	19.40	21.66	17.61	9.98
<i>Coronal (n=750)</i>									
GPT-4o	9.34	3.15	<u>0.96</u>	27.13	58.83	9.27	12.25	10.01	4.31
QWen2.5-VL-7B	13.62	3.54	<u>0.66</u>	37.26	84.19	13.49	14.97	11.47	3.37
ViP-LLaVA	13.85	3.81	0.53	35.21	<u>84.60</u>	12.52	17.07	<u>13.96</u>	3.80
MedFlamingo ✓	10.98	1.66	0.00	17.73	79.98	9.01	11.60	10.34	0.53
MedDr ✓	8.07	2.07	0.29	32.77	76.07	8.09	11.55	9.63	4.08
LLaVA-Med ✓	<u>15.65</u>	4.18	0.68	<u>40.99</u>	84.38	14.18	<u>18.15</u>	13.52	<u>6.54</u>
BiomedGPT ✓	12.60	<u>4.79</u>	0.70	38.47	82.89	<u>15.45</u>	14.78	11.52	4.45
OminiAbnorm-CT ✓	18.38	7.19	2.39	42.88	86.00	19.00	21.30	16.87	9.44
<i>Sagittal (n=591)</i>									
GPT-4o	10.29	3.40	<u>0.84</u>	32.90	72.76	10.07	13.86	11.63	4.04
QWen2.5-VL-7B	13.28	3.54	<u>0.63</u>	35.67	83.98	13.01	14.75	11.34	2.91
ViP-LLaVA	12.84	3.83	0.38	34.51	<u>84.44</u>	11.88	16.29	13.44	2.86
MedFlamingo ✓	10.57	1.53	0.00	17.36	78.87	8.66	11.40	10.14	0.36
MedDr ✓	6.98	1.77	0.28	30.77	75.35	7.12	10.32	8.54	2.42
LLaVA-Med ✓	<u>15.10</u>	4.68	0.66	<u>39.19</u>	84.10	14.18	<u>17.90</u>	<u>13.57</u>	<u>5.11</u>
BiomedGPT ✓	12.59	<u>4.81</u>	0.73	36.62	82.60	<u>15.19</u>	14.62	11.35	3.37
OminiAbnorm-CT ✓	17.29	6.48	1.82	41.77	85.62	17.45	20.43	15.87	7.51

Implementation details. In practice, we adopt QWen2.5-VL-7B [56] as the multi-modal language model, and a 6-layer U-Net as the segmentation module. The cross-attention module consists of 6 layers. As shown in Appendix Section A.8, we find that expanding the input context range (i.e., using more slices) does not enhance the report generation performance of the multi-modal language model. Thus, we only feed the central slice to the model. However, for the segmentation module, we include up to 8 adjacent slices as additional input. To save computational cost, we only optimize the inserted LoRA layers [24] in the multi-modal language model while leaving the whole segmentation module trainable. More implementation details are in Appendix Section A.3.

5 Experiments

In this section, we first present experimental settings in Section 5.1, including task formulation, metrics, baselines, and test datasets. We then provide detailed quantitative experimental results in Section 5.2, and ablation study in Section 5.3. In addition, the qualitative experimental results are in the Appendix Section A.1 and more ablation studies are in the Appendix A.8 and A.9.

5.1 Experiment Settings

Based on OminiAbnorm-CT-14K, we build a rigorous and comprehensive benchmark to evaluate both grounding and description generation abilities for abnormalities on whole-body CT images.

Task formulation. As detailed in Section 3.4, we evaluate methods on three tasks of increasing difficulty: **visual prompted report generation**, **grounded report generation**, and **text-guided grounded report generation**. For text-guided grounded report generation, we generate queries for both present and absent abnormalities at a 3:1 ratio to simulate realistic diagnostic scenarios.

Table 2: **Quantitative results on grounded report generation.** Results are averaged within each category and across all categories, with the best results **bolded** and the second best underlined.

Model	DSC	B-1	B-2	B-3	RTSc	BTSc	MTR	R-1	R-L	RG
<i>Axial (n=2193)</i>										
LiSA + LLaVA-Med	20.96	12.94	6.65	0.73	31.38	82.07	19.20	14.62	12.44	2.79
BiomedParse + LLaVA-Med	15.78	<u>13.61</u>	<u>6.98</u>	<u>0.84</u>	<u>31.50</u>	82.36	<u>19.84</u>	<u>15.28</u>	<u>13.02</u>	2.74
MedULS + LLaVA-Med	15.24	12.70	6.43	0.74	31.05	<u>84.27</u>	18.74	14.67	12.42	2.31
OminiAbnorm-CT	36.04	18.50	11.75	7.90	33.24	86.10	21.83	21.65	18.75	3.78
<i>Coronal (n=750)</i>										
LiSA + LLaVA-Med	17.09	11.48	5.85	0.64	33.28	82.27	16.23	14.36	12.12	2.74
BiomedParse + LLaVA-Med	14.55	<u>11.71</u>	<u>5.95</u>	<u>0.68</u>	32.89	81.80	<u>16.88</u>	<u>14.75</u>	<u>12.57</u>	<u>3.35</u>
MedULS + LLaVA-Med	12.77	11.64	5.88	0.64	32.25	84.11	16.45	14.71	12.34	2.96
OminiAbnorm-CT	31.65	19.13	11.86	7.81	35.47	85.58	20.66	22.14	18.26	4.55
<i>Sagittal (n=591)</i>										
LiSA + LLaVA-Med	14.72	<u>11.10</u>	<u>5.60</u>	<u>0.58</u>	31.51	81.12	<u>16.18</u>	14.07	<u>11.96</u>	<u>2.18</u>
BiomedParse + LLaVA-Med	14.45	10.89	5.46	0.52	<u>32.10</u>	79.37	15.68	14.06	11.95	2.13
MedULS + LLaVA-Med	12.95	10.95	5.32	0.50	30.94	<u>83.53</u>	15.39	<u>14.12</u>	11.83	1.87
OminiAbnorm-CT	34.38	17.10	10.63	7.10	33.13	85.25	19.05	20.92	17.67	3.70

Metrics. For grounding results, we calculate Dice Similarity Coefficient (DSC); for generated descriptions, we calculate BLEU (B) [45], RaTEScore (RTSc) [62], BERTScore (BTSc) [59], ME-TEOR (MTR) [7], ROUGE (R) [35] and RadGraph (RG) [14]. In the text-guided grounded report generation, we prompt models to output a specific response when the queried abnormalities are confirmed absent. Specificity (SP) is then calculated as the proportion of correctly identified absent abnormalities out of all truly absent abnormalities in the test set. Meanwhile, when models miss the queried abnormalities, both DSC and all description metrics are assigned as 0.

Baseline. For visual prompted report generation, we compare with multi-modal LLMs in both the medical domain (MedDr [20], BiomedGPT [58], LLaVA-Med [33], and Med-Flamingo [44]) and the general domain (GPT-4o [25], Qwen2.5-VL [56], and ViP-LLaVA [8]). For (text-guided) grounded report generation, as no such solution exists in the literature, we prompt LLaVA-Med to describe abnormal findings based on segmentation results from auxiliary grounding models. Since the images in OminiAbnorm-CT-14K lack the original DICOM metadata, we only consider 2D segmentation models as baselines, including BiomedParse [61], LiSA [31], and MedULS [13]. More details are in Appendix Section A.4.

Data. We independently split the train and test data for axial, coronal, and sagittal images. To guarantee diversity, we allocate at least 5 samples per category to the axial test set (2 for coronal and sagittal), or all samples if fewer exist, with the remaining data following a 3:1 train-test ratio. To avoid data leakage, images from the same patient are restricted to the same set.

5.2 Experiment Results

Visual Prompted Report Generation. As depicted in Table 1, OminiAbnorm-CT consistently outperforms all baselines across all planes and metrics. Specifically, compared to the strongest baseline LLaVA-Med, OminiAbnorm-CT achieves average improvements of 2.5 in BLEU-1, 2.7 in RaTEScore, and 3.1 in RadGraph across all three planes. These results demonstrate OminiAbnorm-CT’s effectiveness in semi-automated workflows, where radiologists identify abnormalities and the model provides accurate and detailed interpretations.

Grounded Report Generation. As shown in Table 2, OminiAbnorm-CT demonstrates superior grounding capabilities, outperforming the best baselines by 15.08, 14.56, and 19.66 in DSC across axial, coronal, and sagittal planes respectively. For report generation, OminiAbnorm-CT achieves the best performance across all metrics, with notable improvements in both RadGraph and RaTEScore across all anatomical planes, indicating that the generated reports can better align with clinical standards. These results demonstrate OminiAbnorm-CT’s potential for fully automated abnormality localization and report generation in clinical settings.

Text-guided Grounded Report Generation. As shown in Table 3, OminiAbnorm-CT demonstrates superior grounding capabilities, with DSC scores improving by 14.24, 14.14, and 14.54 in axial,

Table 3: **Quantitative results on text-guided grounded report generation.** Results are averaged within each category and then across all categories, with the best **bolded** and the second best underlined.

Model	DSC	SP	B-1	B-2	B-3	RTSc	BTSc	MTR	R-1	R-L	RG
<i>Axial (n=2193)</i>											
MedULS + LLaVA-Med	14.53	6.10	9.54	2.18	0.19	27.35	82.98	11.45	11.48	9.20	1.61
LiSA + LLaVA-Med	<u>17.48</u>	<u>21.35</u>	<u>10.57</u>	<u>2.41</u>	<u>0.28</u>	29.18	<u>83.47</u>	11.59	12.34	9.80	1.61
BiomedParse + LLaVA-Med	16.57	19.87	10.66	2.38	0.26	<u>29.66</u>	83.39	11.74	<u>12.62</u>	<u>9.86</u>	<u>2.16</u>
OminiAbnorm-CT	32.40	58.43	11.94	3.33	0.74	34.80	83.85	12.94	14.65	11.94	4.32
<i>Coronal (n=750)</i>											
MedULS + LLaVA-Med	12.26	5.37	10.73	2.60	<u>0.26</u>	29.34	82.89	11.40	12.79	9.82	1.61
LiSA + LLaVA-Med	12.04	13.76	<u>11.58</u>	<u>2.71</u>	0.22	<u>30.76</u>	<u>83.21</u>	11.36	13.40	10.23	1.83
BiomedParse + LLaVA-Med	<u>13.60</u>	<u>17.79</u>	11.21	2.64	0.25	30.24	83.33	<u>11.47</u>	<u>13.50</u>	<u>10.31</u>	<u>2.34</u>
OminiAbnorm-CT	27.74	45.16	12.51	4.10	1.22	36.56	82.98	13.61	15.83	12.36	5.72
<i>Sagittal (n=591)</i>											
MedULS + LLaVA-Med	11.89	7.66	10.25	2.69	0.29	27.40	82.49	11.24	12.17	9.53	1.23
LiSA + LLaVA-Med	11.23	16.67	<u>11.14</u>	2.72	0.30	29.79	82.88	11.15	13.36	10.07	1.42
BiomedParse + LLaVA-Med	<u>15.35</u>	<u>17.57</u>	11.07	<u>2.72</u>	<u>0.39</u>	<u>31.12</u>	<u>83.01</u>	<u>11.66</u>	<u>13.85</u>	<u>10.40</u>	<u>1.78</u>
OminiAbnorm-CT	29.89	45.41	12.80	4.51	1.42	36.04	83.97	14.02	16.20	12.79	4.85

coronal, and sagittal planes respectively compared to the best baselines. For report generation, OminiAbnorm-CT excels across both lexical overlap metrics (average improvements of 1.3 on BLEU-1 and 2.2 on ROUGE-1 across all planes) and clinical relevance metrics (average gains of 4.0 on RaTEScore and 2.9 on RadGraph across all planes), confirming its superior ability to generate reports that align with clinical assessments. Additionally, OminiAbnorm-CT achieves significantly higher Specificity, demonstrating its robustness to queries about non-existing abnormalities.

5.3 Ablation Study

The integration of the segmentation module allows OminiAbnorm-CT to acquire grounding evidence for abnormal findings and generate descriptions accordingly. To validate its necessity, we conduct an ablation study comparing the full model against a variant where the segmentation module is removed (denoted as OminiAbnorm-CT w/o Seg). This modified version directly generates findings descriptions without anatomical localization guidance.

In the **text-guided grounded report generation task**, as shown in Table 4, OminiAbnorm-CT without the segmentation module demonstrates notable performance degradation, with inferior results on 23 of 27 metrics across three planes. Furthermore, detailed analysis reveals that without the segmentation module, the model struggles to accurately detect the queried abnormalities in CT images, exhibiting a pronounced negative bias that leads to high specificity scores.

Similarly, in the **grounded report generation task**, as depicted in Table 5, removing the segmentation module leads to consistent performance degradation on all the metrics, further confirming that segmentation-based evidence is crucial for generating high-quality medical reports.

Table 4: Ablation study of the segmentation module for **text-guided grounded report generation** task. Results are averaged within each category and then across all categories, with the best **bolded**

Model	SP	B-1	B-2	B-3	RTSc	BTSc	MTR	R-1	R-L	RG
<i>Axial (n=2193)</i>										
OminiAbnorm-CT w/o Seg	95.39	4.50	2.33	1.21	20.53	31.06	7.04	8.50	7.02	7.25
OminiAbnorm-CT	58.43	11.94	3.33	0.74	34.80	83.85	12.94	14.65	11.94	4.32
<i>Coronal (n=750)</i>										
OminiAbnorm-CT w/o Seg	95.71	4.50	2.47	1.27	19.07	28.34	6.27	7.96	6.43	6.17
OminiAbnorm-CT	45.16	12.51	4.10	1.22	36.56	82.98	13.61	15.83	12.36	5.72
<i>Sagittal (n=591)</i>										
OminiAbnorm-CT w/o Seg	92.08	4.17	2.16	1.12	16.62	25.43	5.84	7.06	5.53	5.67
OminiAbnorm-CT	45.41	12.80	4.51	1.42	36.04	83.97	14.02	16.20	12.79	4.85

Table 5: Ablation study of the segmentation module in **grounded report generation** task. Results are averaged within each category and then across all categories, with the best **bolded**

Model	B-1	B-2	B-3	RTSc	BTSc	MTR	R-1	R-L	RG
<i>Axial (n=2193)</i>									
OminiAbnorm-CT w/o Seg	7.73	4.74	3.16	27.87	73.14	17.65	15.18	13.58	3.42
OminiAbnorm-CT	19.00	12.26	8.40	33.85	86.24	22.45	22.27	19.43	4.60
<i>Coronal (n=750)</i>									
OminiAbnorm-CT w/o Seg	8.12	4.81	3.12	31.03	75.55	15.64	15.27	13.23	3.84
OminiAbnorm-CT	19.28	12.03	7.96	35.40	85.56	20.81	22.35	18.47	4.65
<i>Sagittal (n=591)</i>									
OminiAbnorm-CT w/o Seg	8.79	5.21	3.33	31.21	77.41	16.18	15.86	13.87	3.91
OminiAbnorm-CT	16.69	10.41	6.98	33.45	84.94	18.77	20.67	17.61	3.83

6 Related Work

Medical image segmentation aims to delineate clinically meaningful regions on medical images. For radiology images, most datasets focus on annotations for important organs and anatomical structures [52, 47, 40, 29] or lesions [22, 4, 43, 13, 55]. Specialist segmentation models [26, 49, 65, 66] have achieved remarkable success in the past decade, while recently, building foundational generalist models [38, 61, 63, 16] has received increased attention. However, few works contribute to the grounding of abnormal image findings, which encompass a broader spectrum including abnormal organs, potential lesions, and more generally, any anomalies meaningful for clinical decision-making.

Medical image report generation aims to faithfully interpret the medical images with formal text, which is indispensable for numerous clinic procedures [48]. Existing datasets with image-report pairs are limited to specific modalities and regions, such as chest X-ray [30], brain MRI [32] and chest CT [19, 10], overlooking the clinical demands for multi-plane whole-body CT image report generation. Recent progress [60, 12, 32, 11] on grounded report generation are limited to structured organ-level segmentation and description, failing to localize and interpret fine-grained abnormalities.

Generative visual-language foundation models for medicine are built on large-scale multi-modal medical data, and have demonstrated exceptional performance and generalization capabilities across diverse medical tasks [53, 44, 58, 33, 20]. Despite their potential application to multi-plane, whole-body CT images, however, most existing approaches fail to simultaneously provide grounded evidence during generation, leading to poor explainability and hallucinations that are more difficult to detect.

7 Conclusion

This paper advances the automatic grounded interpretation of CT imaging from an abnormality-centric view. To support this, we develop a hierarchical taxonomy of 404 representative abnormal findings on CT images. We contribute **OminiAbnorm-CT-14K**, a meticulously annotated dataset with detailed grounding and description annotation for around 19K abnormalities, from 14.5K multi-plane CT images across the entire human body. Built on this dataset, **OminiAbnorm-CT** enables automatic grounding and description of abnormalities, while supporting flexible clinical usage with text queries or visual prompts. Comprehensive evaluations across three clinically representative tasks demonstrate OminiAbnorm-CTs superior performance. Our work pioneers abnormality-centric CT interpretation, enhancing diagnostic transparency through accurate grounding and detailed characterization of findings, with significant potential to transform radiological practice.

Acknowledgments and Disclosure of Funding

Weidi would like to acknowledge the funding from Scientific Research Innovation Capability Support Project for Young Faculty (ZY-GXQNJSKYCXNLZCXM-I22).

References

- [1] Radiopaedia. <https://radiopaedia.org>, [insert year accessed]. Accessed: [insert access date here].
- [2] Andy Adam, Adrian K. Dixon, Jonathan H. Gillard, and Cornelia Schaefer-Prokop. *Grainger & Allison's Diagnostic Radiology*. Elsevier, 7th edition, 2020.
- [3] AA Ahmed, MM Elmohr, D Fuentes, MA Habra, SB Fisher, ND Perrier, M Zhang, and KM Elsayes. Radiomic mapping model for prediction of ki-67 expression in adrenocortical carcinoma. *Clinical Radiology*, 75(6):479–e17, 2020.
- [4] Michela Antonelli, Annika Reinke, Spyridon Bakas, Keyvan Farahani, Annette Kopp-Schneider, Bennett A Landman, Geert Litjens, Bjoern Menze, Olaf Ronneberger, Ronald M Summers, et al. The medical segmentation decathlon. *Nature communications*, 13(1):4128, 2022.
- [5] Samuel G Armato III, Geoffrey McLennan, Luc Bidaut, Michael F McNitt-Gray, Charles R Meyer, Anthony P Reeves, Binsheng Zhao, Denise R Aberle, Claudia I Henschke, Eric A Hoffman, et al. The lung image database consortium (lidc) and image database resource initiative (idri): a completed reference database of lung nodules on ct scans. *Medical physics*, 38(2):915–931, 2011.
- [6] Shaimaa Bakr, Olivier Gevaert, Sebastian Echegaray, Kelsey Ayers, Mu Zhou, Majid Shafiq, Hong Zheng, Jalen Anthony Benson, Weiruo Zhang, Ann NC Leung, et al. A radiogenomic dataset of non-small cell lung cancer. *Scientific Data*, 5(1):1–9, 2018.
- [7] Satanjeev Banerjee and Alon Lavie. Meteor: An automatic metric for mt evaluation with improved correlation with human judgments. In *Proceedings of the acl workshop on intrinsic and extrinsic evaluation measures for machine translation and/or summarization*, pages 65–72, 2005.
- [8] Mu Cai, Haotian Liu, Siva Karthik Mustikovela, Gregory P Meyer, Yuning Chai, Dennis Park, and Yong Jae Lee. Vip-llava: Making large multimodal models understand arbitrary visual prompts. In *Proceedings of the IEEE Conference on Computer Vision and Pattern Recognition*, pages 12914–12923, 2024.
- [9] Junying Chen, Chi Gui, Ruyi Ouyang, Anningzhe Gao, Shunian Chen, Guiming Hardy Chen, Xidong Wang, Ruifei Zhang, Zhenyang Cai, Ke Ji, et al. Huatuoogpt-vision, towards injecting medical visual knowledge into multimodal llms at scale. *arXiv preprint arXiv:2406.19280*, 2024.
- [10] Yinda Chen, Che Liu, Xiaoyu Liu, Rossella Arcucci, and Zhiwei Xiong. Bimcv-r: A landmark dataset for 3d ct text-image retrieval. In *Medical Image Computing and Computer-Assisted Intervention*, pages 124–134. Springer, 2024.
- [11] Z Chen, M Varma, JB Delbrouck, et al. A vision-language foundation model to enhance efficiency of chest x-ray interpretation. *Preprint at https://arxiv.org/abs/2401.12208*, 2024.
- [12] Zhixuan Chen, Yequan Bie, Haibo Jin, and Hao Chen. Large language model with region-guided referring and grounding for ct report generation. *IEEE Transactions on Medical Imaging*, 2025.
- [13] MJJ de Grauw, E Th Scholten, EJ Smit, MJCM Rutten, M Prokop, B van Ginneken, and A Hering. The uls23 challenge: a baseline model and benchmark dataset for 3d universal lesion segmentation in computed tomography. *arXiv preprint arXiv:2406.05231*, 2024.
- [14] Jean-Benoit Delbrouck, Pierre Chambon, Zhihong Chen, Maya Varma, Andrew Johnston, Louis Blankemeier, Dave Van Veen, Tan Bui, Steven Truong, and Curtis Langlotz. Radgraph-xl: A large-scale expert-annotated dataset for entity and relation extraction from radiology reports. In *Findings of the Association for Computational Linguistics*, pages 12902–12915, 2024.
- [15] Reuben Dorent, Roya Khajavi, Tagwa Idris, Erik Ziegler, Bhanusupriya Somarouthu, Heather Jacene, Ann LaCasce, Jonathan Deissler, Jan Ehrhardt, Sofija Engelson, et al. Lnq 2023 challenge: Benchmark of weakly-supervised techniques for mediastinal lymph node quantification. *arXiv preprint arXiv:2408.10069*, 2024.

- [16] Yuxin Du, Fan Bai, Tiejun Huang, and Bo Zhao. Segvol: Universal and interactive volumetric medical image segmentation. *Advances in Neural Information Processing Systems*, 37:110746–110783, 2024.
- [17] Henry Gray and S Standring. *Gray’s anatomy*. Arcturus Publishing London, 2008.
- [18] John R. Haaga and Daniel Boll. *CT and MRI of the Whole Body, 2-Volume Set*. Elsevier, 6th edition, 2016.
- [19] Ibrahim Ethem Hamamci, Sezgin Er, Furkan Almas, Ayse Gulnihan Simsek, Sevvil Nil Esirgun, Irem Dogan, Muhammed Furkan Dasdelen, Bastian Wittmann, Enis Simsar, Mehmet Simsar, et al. A foundation model utilizing chest ct volumes and radiology reports for supervised-level zero-shot detection of abnormalities. *CoRR*, 2024.
- [20] Sunan He, Yuxiang Nie, Zhixuan Chen, Zhiyuan Cai, Hongmei Wang, Shu Yang, and Hao Chen. Meddr: Diagnosis-guided bootstrapping for large-scale medical vision-language learning. *arXiv preprint arXiv:2404.15127*, 2024.
- [21] Yuting He, Guanyu Yang, Jian Yang, Rongjun Ge, Youyong Kong, Xiaomei Zhu, Shaobo Zhang, Pengfei Shao, Huazhong Shu, Jean-Louis Dillenseger, et al. Meta grayscale adaptive network for 3d integrated renal structures segmentation. *Medical image analysis*, 71:102055, 2021.
- [22] Nicholas Heller, Fabian Isensee, Darya Trofimova, Resha Tejpal, Nikolaos Papanikolopoulos, and Christopher Weight. Kidney and kidney tumor segmentation. Springer, 2021.
- [23] Nicholas Heller, Fabian Isensee, Dasha Trofimova, Resha Tejpal, Zhongchen Zhao, Huai Chen, Lisheng Wang, Alex Golts, Daniel Khapun, Daniel Shats, et al. The kits21 challenge: Automatic segmentation of kidneys, renal tumors, and renal cysts in corticomedullary-phase ct. *arXiv preprint arXiv:2307.01984*, 2023.
- [24] Edward J Hu, Yelong Shen, Phillip Wallis, Zeyuan Allen-Zhu, Yuanzhi Li, Shean Wang, Lu Wang, Weizhu Chen, et al. Lora: Low-rank adaptation of large language models. 1(2):3, 2022.
- [25] Aaron Hurst, Adam Lerer, Adam P Goucher, Adam Perelman, Aditya Ramesh, Aidan Clark, AJ Ostrow, Akila Welihinda, Alan Hayes, Alec Radford, et al. Gpt-4o system card. *arXiv preprint arXiv:2410.21276*, 2024.
- [26] Fabian Isensee, Paul F Jaeger, Simon AA Kohl, Jens Petersen, and Klaus H Maier-Hein. nnu-net: a self-configuring method for deep learning-based biomedical image segmentation. *Nature Methods*, 18(2):203–211, 2021.
- [27] Fabian Isensee, Maximilian Rokuss, Lars Krämer, Stefan Dinkelacker, Ashis Ravindran, Florian Stritzke, Benjamin Hamm, Tassilo Wald, Moritz Langenberg, Constantin Ulrich, et al. nninteractive: Redefining 3d promptable segmentation. *arXiv preprint arXiv:2503.08373*, 2025.
- [28] Alexander Jaus, Constantin Seibold, Kelsey Hermann, Alexandra Walter, Kristina Giske, Johannes Haubold, Jens Kleesiek, and Rainer Stiefelhagen. Towards unifying anatomy segmentation: automated generation of a full-body ct dataset via knowledge aggregation and anatomical guidelines. *arXiv preprint arXiv:2307.13375*, 2023.
- [29] Yuanfeng Ji, Haotian Bai, Chongjian Ge, Jie Yang, Ye Zhu, Ruimao Zhang, Zhen Li, Lingyan Zhanng, Wanling Ma, Xiang Wan, et al. Amos: A large-scale abdominal multi-organ benchmark for versatile medical image segmentation. *Advances in Neural Information Processing Systems*, 35:36722–36732, 2022.
- [30] Alistair EW Johnson, Tom J Pollard, Seth J Berkowitz, Nathaniel R Greenbaum, Matthew P Lungren, Chih-ying Deng, Roger G Mark, and Steven Horng. Mimic-cxr, a de-identified publicly available database of chest radiographs with free-text reports. *Scientific data*, 6(1):317, 2019.
- [31] Xin Lai, Zhuotao Tian, Yukang Chen, Yanwei Li, Yuhui Yuan, Shu Liu, and Jiaya Jia. Lisa: Reasoning segmentation via large language model. In *Proceedings of the IEEE Conference on Computer Vision and Pattern Recognition*, pages 9579–9589, 2024.

- [32] Jiayu Lei, Xiaoman Zhang, Chaoyi Wu, Lisong Dai, Ya Zhang, Yanyong Zhang, Yanfeng Wang, Weidi Xie, and Yuehua Li. Autorg-brain: Grounded report generation for brain mri. *arXiv preprint arXiv:2407.16684*, 2024.
- [33] Chunyuan Li, Cliff Wong, Sheng Zhang, Naoto Usuyama, Haotian Liu, Jianwei Yang, Tristan Naumann, Hoifung Poon, and Jianfeng Gao. Llava-med: Training a large language-and-vision assistant for biomedicine in one day. *Advances in Neural Information Processing Systems*, 36:28541–28564, 2023.
- [34] Xiangyu Li, Gongning Luo, Kuanquan Wang, Hongyu Wang, Jun Liu, Xinjie Liang, Jie Jiang, Zhenghao Song, Chunyue Zheng, Haokai Chi, et al. The state-of-the-art 3d anisotropic intracranial hemorrhage segmentation on non-contrast head ct: The instance challenge. *arXiv preprint arXiv:2301.03281*, 2023.
- [35] Chin-Yew Lin. Rouge: A package for automatic evaluation of summaries. In *Text summarization branches out*, pages 74–81, 2004.
- [36] Ilya Loshchilov and Frank Hutter. Decoupled weight decay regularization. *arXiv preprint arXiv:1711.05101*, 2017.
- [37] Xiangde Luo, Jia Fu, Yunxin Zhong, Shuolin Liu, Bing Han, Mehdi Astaraki, Simone Bendazzoli, Iuliana Toma-Dasu, Yiwen Ye, Ziyang Chen, et al. Segrap2023: A benchmark of organs-at-risk and gross tumor volume segmentation for radiotherapy planning of nasopharyngeal carcinoma. *Medical Image Analysis*, page 103447, 2025.
- [38] Jun Ma, Yuting He, Feifei Li, Lin Han, Chenyu You, and Bo Wang. Segment anything in medical images. *Nature Communications*, 15(1):654, 2024.
- [39] Jun Ma, Yixin Wang, Xingle An, Cheng Ge, Ziqi Yu, Jianan Chen, Qiongjie Zhu, Guoqiang Dong, Jian He, Zhiqiang He, et al. Toward data-efficient learning: A benchmark for covid-19 ct lung and infection segmentation. *Medical physics*, 48(3):1197–1210, 2021.
- [40] Jun Ma, Yao Zhang, Song Gu, Cheng Ge, Shihao Mae, Adamo Young, Cheng Zhu, Xin Yang, Kangkang Meng, Ziyang Huang, et al. Unleashing the strengths of unlabelled data in deep learning-assisted pan-cancer abdominal organ quantification: the flare22 challenge. *The Lancet Digital Health*, 6(11):e815–e826, 2024.
- [41] Jacob Mandell. *Core Radiology: A Visual Approach to Diagnostic Imaging*. Cambridge University Press, 2013.
- [42] Mojtaba Masoudi, Hamid-Reza Pourreza, Mahdi Saadatmand-Tarzjan, Noushin Eftekhari, Fateme Shafiee Zargar, and Masoud Pezeshki Rad. A new dataset of computed-tomography angiography images for computer-aided detection of pulmonary embolism. *Scientific Data*, 5, 2018.
- [43] Bjoern H Menze, Andras Jakab, Stefan Bauer, Jayashree Kalpathy-Cramer, Keyvan Farahani, Justin Kirby, Yuliya Burren, Nicole Porz, Johannes Slotboom, Roland Wiest, et al. The multimodal brain tumor image segmentation benchmark (brats). *IEEE transactions on medical imaging*, 34(10):1993–2024, 2014.
- [44] Michael Moor, Qian Huang, Shirley Wu, Michihiro Yasunaga, Yash Dalmia, Jure Leskovec, Cyril Zakka, Eduardo Pontes Reis, and Pranav Rajpurkar. Med-flamingo: a multimodal medical few-shot learner. In *Machine Learning for Health (ML4H)*, pages 353–367. PMLR, 2023.
- [45] Kishore Papineni, Salim Roukos, Todd Ward, and Wei-Jing Zhu. Bleu: a method for automatic evaluation of machine translation. In *Association for Computational Linguistics*, pages 311–318, 2002.
- [46] João Pedrosa, Guilherme Aresta, Carlos Ferreira, Gurraj Atwal, Hady Ahmady Phoulady, Xiaoyu Chen, Rongzhen Chen, Jiaoliang Li, Liansheng Wang, Adrian Galdran, et al. Lndb challenge on automatic lung cancer patient management. *Medical image analysis*, 70:102027, 2021.

- [47] Chongyu Qu, Tiezheng Zhang, Hualin Qiao, Yucheng Tang, Alan L Yuille, Zongwei Zhou, et al. Abdomenatlas-8k: Annotating 8,000 ct volumes for multi-organ segmentation in three weeks. *Advances in Neural Information Processing Systems*, 36, 2023.
- [48] Vishwanatha M Rao, Michael Hla, Michael Moor, Subathra Adithan, Stephen Kwak, Eric J Topol, and Pranav Rajpurkar. Multimodal generative ai for medical image interpretation. *Nature*, 639(8056):888–896, 2025.
- [49] Olaf Ronneberger, Philipp Fischer, and Thomas Brox. U-net: Convolutional networks for biomedical image segmentation. In *Medical Image Computing and Computer-Assisted Intervention*, pages 234–241. Springer, 2015.
- [50] Holger R Roth, Le Lu, Ari Seff, Kevin M Cherry, Joanne Hoffman, Shijun Wang, Jiamin Liu, Evrim Turkbey, and Ronald M Summers. A new 2.5 d representation for lymph node detection using random sets of deep convolutional neural network observations. In *Medical Image Computing and Computer-Assisted Intervention*, pages 520–527. Springer, 2014.
- [51] T. Urban, E. Ziegler, S. Pieper, J. Kirby, D. Rukas, B. Beardmore, B. Somarouthu, E. Ozkan, G. Lelis, B. Fevrier-Sullivan, S. Nandekar, A. Beers, C. Jaffe, J. Freymann, D. Clunie, G. J. Harris, and J. Kalpathy-Cramer. Crowds cure cancer: Crowdsourced data collected at the rsna 2018 annual meeting, 2019.
- [52] Jakob Wasserthal, Hanns-Christian Breit, Manfred T Meyer, Maurice Pradella, Daniel Hinck, Alexander W Sauter, Tobias Heye, Daniel T Boll, Joshy Cyriac, Shan Yang, et al. Totalsegmentator: Robust segmentation of 104 anatomic structures in ct images. *Radiology: Artificial Intelligence*, 5(5), 2023.
- [53] Chaoyi Wu, Xiaoman Zhang, Ya Zhang, Yanfeng Wang, and Weidi Xie. Towards generalist foundation model for radiology by leveraging web-scale 2d&3d medical data. *arXiv preprint arXiv:2308.02463*, 2023.
- [54] Haoning Wu, Ziheng Zhao, Ya Zhang, Weidi Xie, and Yanfeng Wang. Mrgen: Diffusion-based controllable data engine for mri segmentation towards unannotated modalities. *arXiv preprint arXiv:2412.04106*, 2024.
- [55] Ke Yan, Xiaosong Wang, Le Lu, Ling Zhang, Adam P Harrison, Mohammadhadi Bagheri, and Ronald M Summers. Deep lesion graphs in the wild: relationship learning and organization of significant radiology image findings in a diverse large-scale lesion database. In *Proceedings of the IEEE Conference on Computer Vision and Pattern Recognition*, 2018.
- [56] An Yang, Baosong Yang, Beichen Zhang, Binyuan Hui, Bo Zheng, Bowen Yu, Chengyuan Li, Dayiheng Liu, Fei Huang, Haoran Wei, et al. Qwen2. 5 technical report. *arXiv preprint arXiv:2412.15115*, 2024.
- [57] Jiancheng Yang, Rui Shi, Liang Jin, Xiaoyang Huang, Kaiming Kuang, Donglai Wei, Shixuan Gu, Jianying Liu, Pengfei Liu, Zhizhong Chai, Yongjie Xiao, Hao Chen, Liming Xu, Bang Du, Xiangyi Yan, Hao Tang, Adam Alessio, Gregory Holste, Jiapeng Zhang, Xiaoming Wang, Jianye He, Lixuan Che, Hanspeter Pfister, Ming Li, and Bingbing Ni. Deep rib fracture instance segmentation and classification from ct on the ribfrac challenge. *IEEE Transactions on Medical Imaging*, 2025.
- [58] Kai Zhang, Rong Zhou, Eashan Adhikarla, Zhiling Yan, Yixin Liu, Jun Yu, Zhengliang Liu, Xun Chen, Brian D Davison, Hui Ren, et al. A generalist vision–language foundation model for diverse biomedical tasks. *Nature Medicine*, pages 1–13, 2024.
- [59] Tianyi Zhang, Varsha Kishore, Felix Wu, Kilian Q Weinberger, and Yoav Artzi. Bertscore: Evaluating text generation with bert. In *Proceedings of the International Conference on Learning Representations*.
- [60] Xiaoman Zhang, Chaoyi Wu, Ziheng Zhao, Jiayu Lei, Ya Zhang, Yanfeng Wang, and Weidi Xie. Radgenome-chest ct: A grounded vision-language dataset for chest ct analysis. *arXiv preprint arXiv:2404.16754*, 2024.

- [61] Theodore Zhao, Yu Gu, Jianwei Yang, Naoto Usuyama, Ho Hin Lee, Sid Kiblawi, Tristan Naumann, Jianfeng Gao, Angela Crabtree, Jacob Abel, et al. A foundation model for joint segmentation, detection and recognition of biomedical objects across nine modalities. *Nature Methods*, pages 1–11, 2024.
- [62] Weike Zhao, Chaoyi Wu, Xiaoman Zhang, Ya Zhang, Yanfeng Wang, and Weidi Xie. Ratescore: A metric for radiology report generation. *Proceedings of the Conference on Empirical Methods in Natural Language Processing*, 2024.
- [63] Ziheng Zhao, Yao Zhang, Chaoyi Wu, Xiaoman Zhang, Ya Zhang, Yanfeng Wang, and Weidi Xie. One model to rule them all: Towards universal segmentation for medical images with text prompts. *arXiv preprint arXiv:2312.17183*, 2023.
- [64] Qiaoyu Zheng, Weike Zhao, Chaoyi Wu, Xiaoman Zhang, Lisong Dai, Hengyu Guan, Yuehua Li, Ya Zhang, Yanfeng Wang, and Weidi Xie. Large-scale long-tailed disease diagnosis on radiology images. *Nature Communications*, 15(1):10147, 2024.
- [65] Hong-Yu Zhou, Jiansen Guo, Yinghao Zhang, Xiaoguang Han, Lequan Yu, Liansheng Wang, and Yizhou Yu. nnformer: volumetric medical image segmentation via a 3d transformer. *IEEE Transactions on Image Processing*, 2023.
- [66] Zongwei Zhou, Md Mahfuzur Rahman Siddiquee, Nima Tajbakhsh, and Jianming Liang. Unet++: Redesigning skip connections to exploit multiscale features in image segmentation. *IEEE Transactions on Medical Imaging*, 39(6):1856–1867, 2019.

A Appendix

Contents

1	Introduction	1
2	Taxonomy for Abnormal Findings	3
3	Dataset Curation	3
3.1	Limitation in Existing Datasets	3
3.2	Data Source	4
3.3	Annotation Pipeline	4
3.4	Extension to Instruction Data	4
3.5	Summary	5
4	OminiAbnorm-CT	5
4.1	Problem Formulation	5
4.2	Architecture	5
4.3	Training	6
5	Experiments	7
5.1	Experiment Settings	7
5.2	Experiment Results	8
5.3	Ablation Study	9
6	Related Work	10
7	Conclusion	10
A	Appendix	16
A.1	Qualitative Experiment Results	17
A.2	Limitations	20
A.3	More Implementation Details of OminiAbnorm-CT	20
A.4	Implementation Details of Baselines	21
A.5	Quality Verification on OminiAbnorm-CT-14K	21
A.6	The Long-Tail Distribution of OminiAbnorm-CT-14K	22
A.7	Comparison between OminiAbnorm-CT-14K and Existing Datasets	22
A.8	Ablation Study on Context Range	22
A.9	Ablation Study on Different Visual Prompts	23
A.10	Generation of Text Queries and Visual Prompts	25
A.11	Detailed Distribution of Abnormalities in OminiAbnorm-CT-14K	26

A.1 Qualitative Experiment Results

Fig. 4 presents several examples from the **grounded report generation** task, comparing the segmentation and report generation results between OmniAbnorm-CT and BiomedParse+LLaVA-Med. The results clearly demonstrate that BiomedParse fails to detect any abnormalities in the latter two cases, consequently leading LLaVA-Med to generate reports that are hardly relevant to the images. In contrast, OmniAbnorm-CT successfully localizes the abnormal regions across all examples and produces comparatively more accurate reports for the abnormalities.

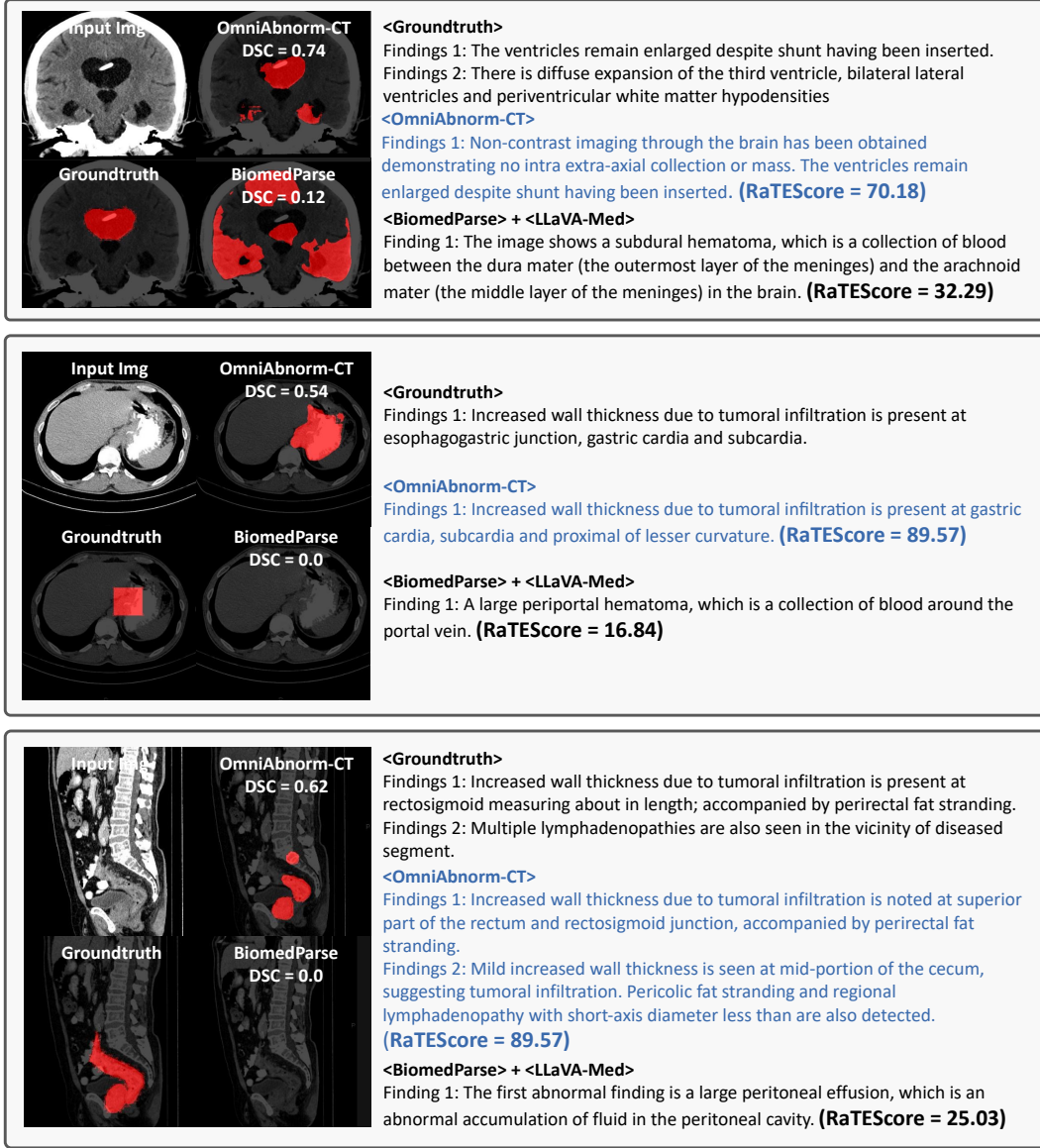


Figure 4: Qualitative comparison on the grounded report generation task.

In Fig. 5, we demonstrate several examples from the **text-guided grounded report generation** task, and compare the segmentation and report generation results of OmniAbnorm-CT and BiomedParse+LLaVA-Med. As illustrated in the first two examples, BiomedParse fails to accurately localize the queried abnormalities. While in the latter two examples, LLaVA-Med is unable to correctly interpret the segmentation results when generating reports. In contrast, OmniAbnorm-CT can successfully localize the queried abnormalities across all examples and generates more precise and clinically relevant reports.

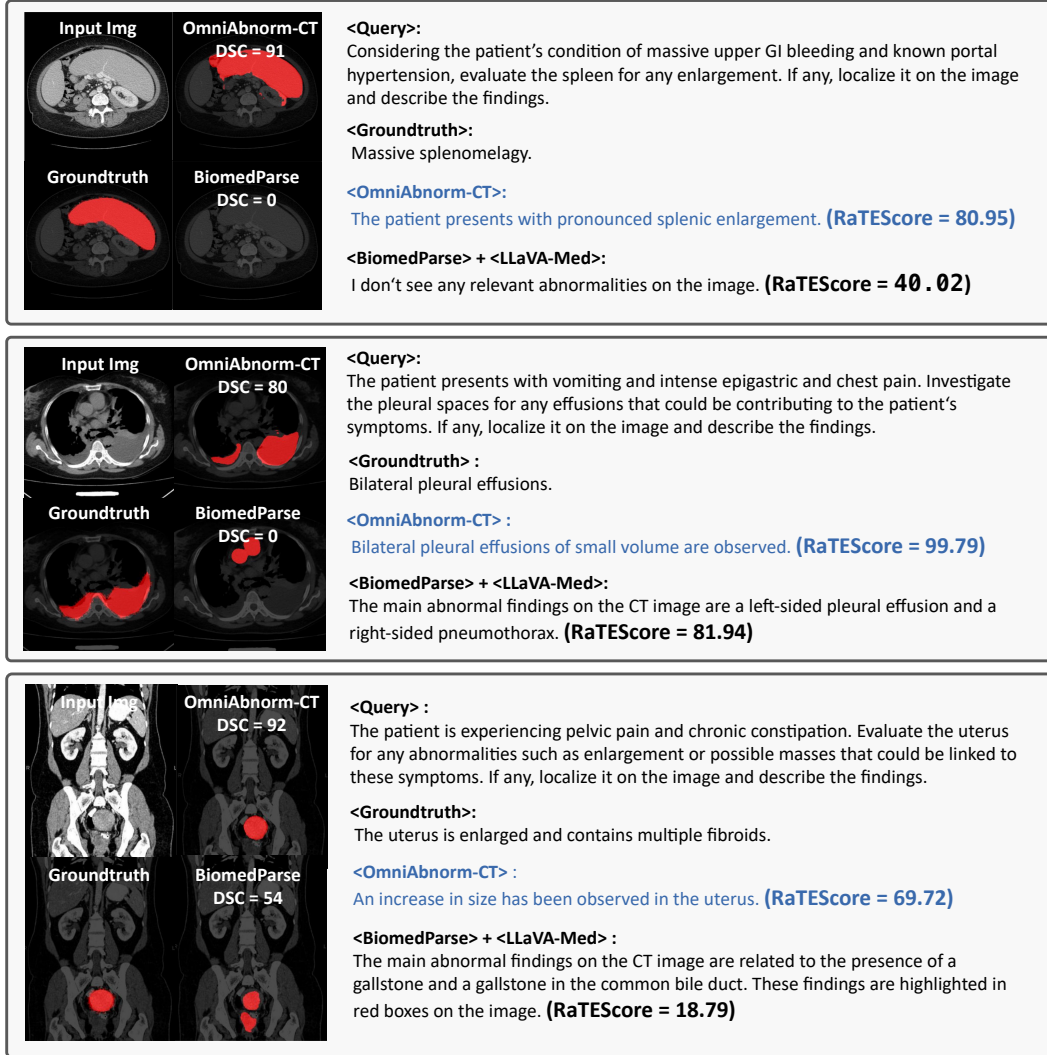


Figure 5: Qualitative comparison on the text-guided grounded report generation task.

In Fig. 6, we demonstrate several representative examples in the **visual prompted report generation** task, comparing the abnormality descriptions generated by OmniAbnorm-CT, LLaVA-Med, and QWen2.5-VL-7B. It shows that LLaVA-Med and QWen2.5-VL-7B exhibit some fundamental errors in their results. For instance, in the first case, LLaVA-Med misidentifies the kidney as the gallbladder; While in the last case, QWen2.5-VL-7B fails to distinguish between the liver and gallbladder. By contrast, OmniAbnorm-CT is able to precisely capture and identify the abnormal findings highlighted by the visual prompts and generate high quality reports.



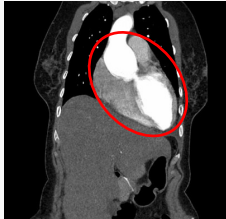
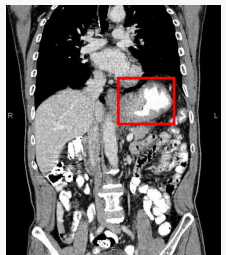
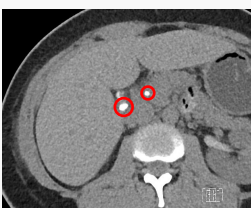
<p>Input Image:</p> 	<p><Groundtruth> : A simple cortical cyst is noted in the left kidney.</p> <p><OminiAbnorm-CT> : The kidneys exhibit several uncomplicated cortical cysts that do not show enhancement. (RaTEScore = 81.03)</p> <p><LLaVA-Med> : The main findings indicated by the red box in this CT image are a dilated gallbladder and a dilated common bile duct. (RaTEScore = 23.09)</p> <p><QWen2.5-VL-7B> : The red box highlights an area of increased density within the mesenteric fat, suggesting the presence of a mesenteric lymph node or a similar soft tissue mass. Further evaluation is recommended for definitive diagnosis. (RaTEScore = 25.01)</p>
<p>Input Image:</p> 	<p><Groundtruth> : Degenerative changes and osteophytosis are seen at the lumbar spine.</p> <p><OminiAbnorm-CT> : Osteophytes indicate degenerative changes present at the lumbar spine levels. (RaTEScore = 87.07)</p> <p><LLaVA-Med> : The main findings indicated by the red-outlined area in the image are a fracture of the L1 vertebra and a fracture of the right sacroiliac joint. (RaTEScore = 27.87)</p> <p><QWen2.5-VL-7B> : The red-outlined area indicates a region of increased density within the vertebral body, suggestive of lytic lesion. Further clinical correlation is necessary for definitive diagnosis. (RaTEScore = 23.83)</p>
<p>Input Image:</p> 	<p><Groundtruth> : Gross cardiomegaly</p> <p><OminiAbnorm-CT> : The patient presents with an enlargement of the heart, indicative of cardiomegaly. (RaTEScore = 81.88)</p> <p><LLaVA-Med> : The main findings indicated by the red circular/elliptical demarcation in the image are a large pericardial effusion and a large pericardial mass. (RaTEScore = 42.35)</p> <p><QWen2.5-VL-7B> : The red circular/elliptical demarcation highlights an area of increased density within the mediastinum, which appears to be consistent with a mass or lesion. Further evaluation is required for definitive diagnosis. (RaTEScore = 29.38)</p>
<p>Input Image:</p> 	<p><Groundtruth> : Marked increased wall thickness due to tumoral infiltration is present at gastric body and antrum accompanied by several regional lymphadenopathies.</p> <p><OminiAbnorm-CT> : Increased wall thickness due to tumoral infiltration is present at gastric cardia and body accompanied by perigastric fat stranding. (RaTEScore = 83.88)</p> <p><LLaVA-Med> : The main findings indicated by the red box in this CT image are a dilated stomach and a dilated duodenum. (RaTEScore = 42.81)</p> <p><QWen2.5-VL-7B> : The red box highlights an area of increased density within the liver parenchyma, suggesting a possible focal lesion. Further characterization is required for definitive diagnosis. (RaTEScore = 39.78)</p>
<p>Input Image:</p> 	<p><Groundtruth> : Small right pleural effusion.</p> <p><OminiAbnorm-CT> : Minimal pleural effusion mainly on the right. (RaTEScore = 85.64)</p> <p><LLaVA-Med> : The main findings indicated by the red-outlined area in the image are a large pericardial effusion and a moderate-sized pleural effusion. (RaTEScore = 34.89)</p> <p><QWen2.5-VL-7B> : The red-outlined area appears to be a normal lung. (RaTEScore = 20.80)</p>
<p>Input Image:</p> 	<p><Groundtruth> : The gallbladder is not abnormally distended and shows multiple gallstones.</p> <p><OminiAbnorm-CT> : Numerous gallstones identified within the gallbladder. (RaTEScore = 88.13)</p> <p><LLaVA-Med> : The main findings indicated by the red-outlined area in the image are a dilated common bile duct (CBD) and a gallstone. (RaTEScore = 59.10)</p> <p><QWen2.5-VL-7B> : The red-outlined area indicates a small, well-defined, hypodense lesion within the liver parenchyma. The lesion appears to be homogenous in density and does not show significant enhancement on this particular phase of contrast administration. Further imaging or clinical correlation is recommended for definitive diagnosis. (RaTEScore = 23.78)</p>

Figure 6: Qualitative comparison on the visual prompted report generation task.

A.2 Limitations

As a pioneering attempt toward automatic grounding and interpretation of abnormalities on multi-plane and whole-body CT images, our work certainly has several limitations: (i) Regarding data annotation, despite providing a large-scale dataset, some rare abnormalities (55 out of 404 in the taxonomy) remain uncovered, as shown in Section A.11. Additionally, many abnormalities have very few annotations, which significantly restricts the model’s capability range. Expanding annotations for these rare categories is treated as our future work. Meanwhile, the CT images in OminiAbnorm-CT-14K may also exhibit demographic and regional bias. (ii) Due to resource constraints, we currently provide grounding annotation for a few representative slices on each CT image, rather than full volumetric segmentation. In the future, we could potentially address this limitation by using interactive segmentation models such as nnInteractive [27]. (iii) Limited by the 3D image perception capability of multi-modal language models, which is also a common challenge in current generative visual-language foundation models for medicine [53, 44, 58, 33, 20], we only considered single slice as input when generating reports. Enhancing models’ ability to reason across adjacent slices and integrate volumetric context represents a critical direction for our future research.

A.3 More Implementation Details of OminiAbnorm-CT

Training Hyperparameters. We adopt 8 NVIDIA A100-80G GPUs for training, with 1 sample per device and gradient accumulation set to 4. We train OminiAbnorm-CT for 250K iterations in total, and use 5% steps for warming up. We take AdamW [36] as optimizer with a learning rate of $2e-4$. When optimizing the multi-modal language model and the segmentation module jointly, we assign equal weights to the text generation loss and segmentation loss, as defined in Equation 7. We set the rank of LORA to 32.

Training Data. We pad and rescale all images to 512×512 . For training data sampling from four tasks: visual prompted report generation, grounded report generation, text-guided grounded report generation, and general VQA, we control the ratio to be 1:1:1:1. Additionally, in the abnormality grounding task, we maintain a ratio of 6:4 between OminiAbnorm-CT-14K and public lesion segmentation data. For each abnormality description, we use the following prompt to have GPT rewrite three different versions, then randomly select one as the ground truth:

Your task is to produce THREE different rewrites of medical reports while preserving all original medical content and diagnostic information, changing only the expression style and sentence structure.

Rules:

1. Strictly maintain all medical information, diagnostic results, numerical values, and key findings.
2. Do not add any new medical content or conclusions.
3. Do not remove any medical information from the original report.
4. Only change the wording, sentence structure, word order, and vocabulary choices.
5. Maintain professional medical language and terminology.
6. Preserve the overall structure of the original report (such as section divisions).
7. Ensure all rewritten reports remain medically rigorous and accurate.
8. Create THREE distinct rewrites with different phrasing and structure.

Input: Original medical report written by a doctor

Output: THREE rewritten versions with identical content but different expression

Please rewrite the following medical report in three different ways:

\$Findings Description\$

Your response must follow this exact format:

\$Output Template\$

A.4 Implementation Details of Baselines

In **visual prompted generation** task, we prompt each abnormality with all types of visual prompts, and take the maximum score. All the methods are prompted with the following template:

You are a helpful medical assistant. Describe the abnormal findings indicated by the \$Visual Prompt\$.

Please use precise medical terminology, maintain the concise reporting style used in formal radiology reports and provide only the specific radiological findings. Do not list general possibilities, explanations, or recommendations.

In **grounded report generation** task, we integrate LLaVA-Med with 2D segmentation models as baselines. Specifically, we re-implement the MedULS [13] with a 2D nnU-Net [26] and the public lesion segmentation datasets in Table 6, covering all the datasets in the official ULS-23 challenge and 10 additional ones. To our knowledge, this represents the segmentation model with the broadest capability range (in terms of abnormality variety) that can be constructed from currently available public datasets. For BiomedParse [61] and LiSA [31], we prompt them with ‘Abnormal findings on the CT image’ to derive segmentation results for all the abnormalities on the input CT image. Then, we combine each segmentation model with LLaVA-Med by converting the segmentation results into bounding boxes overlaid on the CT image, and prompt LLaVA-Med to generate the report based on these visual cues:

You are a helpful medical assistant. The abnormal findings are highlighted in red boxes on this CT image, if present.

Please describe each abnormal finding indicated by the red boxes using the format ‘Finding 1: [description]’, ‘Finding 2: [description]’, etc.

Use precise medical terminology, maintain the concise reporting style used in formal radiology reports and provide only the specific radiological findings. Do not list general possibilities, explanations, or recommendations. Respond with ‘I don’t see any abnormalities on the image.’ if no abnormalities are present.

In **text-guided grounded report generation** task, we use the simulated text queries as prompts for BiomedParse and LiSA to derive segmentation results for the queried abnormalities, which are detailed in Section 3.4. For MedULS, since it doesn’t support text-prompted segmentation, we simply use its unconditioned segmentation results. Similarly, we convert their segmentation results into bounding boxes overlaid on the CT image, and prompt LLaVA-Med to generate the report based on them:

You are a helpful medical assistant. The abnormal findings are highlighted in red boxes on this CT image, if present.

Please describe the abnormal findings indicated by the red boxes.

Use precise medical terminology, maintain the concise reporting style used in formal radiology reports and provide only the specific radiological findings. Do not list general possibilities, explanations, or recommendations. Respond with ‘I don’t see any relevant abnormalities on the image.’ if no abnormalities are present.

A.5 Quality Verification on OminiAbnorm-CT-14K

We conducted rigorous and comprehensive quality verification on the annotations in OminiAbnorm-CT-14K. For each annotator, we randomly sampled 100 annotated images on the axial plane, 50 on the coronal, and 50 on the sagittal plane. Then a senior radiologist with 12 years of experience assesses the annotation quality on four key metrics: (i) **Detection rate** measures the percentage of abnormalities successfully identified and annotated by the annotator, without any omission; (ii) **Grounding precision** evaluates the percentage of grounding annotations that properly encompass the primary regions of the abnormality, while minimizing false positive areas; (iii) **Report concordance** quantifies the percentage of description annotations that faithfully reflect the linked abnormal findings

on the image; (iv) **Classification accuracy** measures the percentage of abnormalities that are correctly categorized.

Our verification results demonstrated that: (i) 3 out of 4 annotators achieved perfect scores across all four metrics (100%). (ii) Only one annotator had 10 abnormality annotations where the descriptions were not sufficiently accurate and the category labels were also incorrect, resulting in Report concordance and Classification accuracy of 95%, while maintaining 100% Detection rate and Grounding precision. These results confirm the high quality of annotations in our OminiAbnorm-CT-14K.

A.6 The Long-Tail Distribution of OminiAbnorm-CT-14K

To mitigate the long-tail distribution in OminiAbnorm-CT-14K, we identified underrepresented organs in our annotated corpus and strategically employed GPT-4o to analyze unlabeled reports. Using the following prompt, we efficiently filtered cases containing abnormal findings related to these underrepresented organs:

This is a report of a CT scan: \$Report\$
Please help me carefully check if the report mentions any abnormal findings that belong to the following anatomical areas: \$List of Underrepresented Organs\$.
If there are, please output 'YES', otherwise output 'NO'. Do not output any other information.

These identified cases were then prioritized in our annotation pipeline. To evaluate the effectiveness of this strategy, we randomly sampled 1,000 images before and after implementation. As shown in Fig. 7, prior to our intervention, the top 20 organs (out of 82 total) accounted for 79.8% of all annotations, while the top 85 abnormality categories (out of 340 total) constituted 80.1%. Following our strategy, the underrepresented organs and rare abnormality categories received notably increased annotation coverage: the representation of underrepresented organs increased by 19.6%, while rare abnormality categories increased by 11.6%, significantly enhancing the diversity of our dataset.

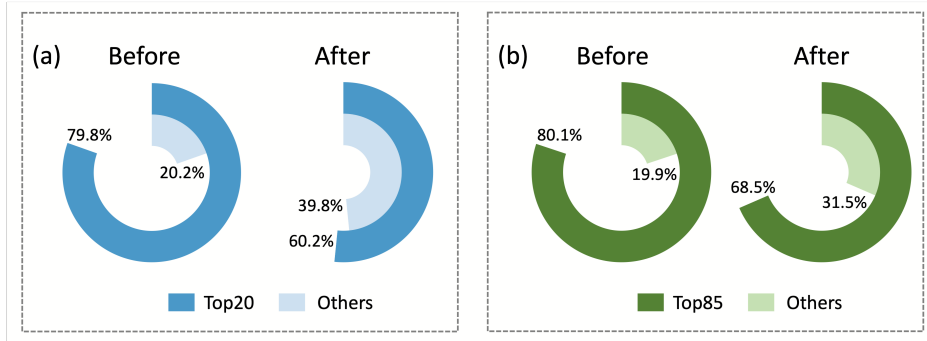


Figure 7: The distribution before and after prioritizing annotation for underrepresented organs. (a) Comparison of organ distribution in annotations; (b) Comparison of abnormality category distribution in annotations.

A.7 Comparison between OminiAbnorm-CT-14K and Existing Datasets

We compare OminiAbnorm-CT-14K with existing public CT image datasets in Table 6, including those widely used for lesion segmentation, lesion detection, organ segmentation, or report generation. In contrast to the substantial limitations exhibited by these datasets, as detailed in Sec. 3.1, OminiAbnorm-CT-14K represents the first large-scale dataset designed for abnormality grounding and description across multi-plane and whole-body CT images.

A.8 Ablation Study on Context Range

In clinical practice, the contextual information provided by adjacent slices is critical for the interpretation of CT images, which is also widely validated in tasks such as medical image segmentation [26] and diagnosis [64]. To investigate the impact of context range on report generation, in the visual prompted report generation task, we adjust the number of input slices and evaluate its impact on a

Table 6: Comparison of key characteristics between OminiAbnorm-CT-14K and widely-used public CT imaging datasets. Note that CCC18 and DeepLesion has no category label for each annotated lesion. Even though some scans in these datasets are isotropic, they are acquired as axial-plane. Abbreviations: Rpt = Report; Cat = Abnormality Category; Img = Image; Seg. = Segmentation; Det. = Detection; Gen = Generation.

Dataset	Task	Anatomy	Plane	Rpt	#Cat	#Img
ULS Bone [13]	Lesion Seg.	Bone	Axial	✗	1	151
ULS Pancreas [13]	Lesion Seg.	Pancreas	Axial	✗	1	119
MSD Liver [4]	Lesion Seg.	Liver	Axial	✗	1	131
MSD Lung [4]	Lesion Seg.	Lung	Axial	✗	1	63
MSD Colon [4]	Lesion Seg.	Colon	Axial	✗	1	126
MSD Pancreas [4]	Lesion Seg.	Pancreas	Axial	✗	1	281
COVID19 [39]	Lesion Seg.	Lung	Axial	✗	1	20
KiTS23 [23]	Lesion Seg.	Kidney	Axial	✗	2	489
KiPA22 [21]	Lesion Seg.	Kidney	Axial	✗	2	70
NSCLC [6]	Lesion Seg.	Lung	Axial	✗	1	85
LIDC IDRI [5]	Lesion Seg.	Lung	Axial	✗	1	750
LNDb [46]	Lesion Seg.	Lung	Axial	✗	1	236
INSTANCE22 [34]	Lesion Seg.	Brain	Axial	✗	1	100
Seg.Rap2023 [37]	Lesion Seg.	Head & Neck	Axial	✗	2	120
FUMPE [42]	Lesion Seg.	Lung	Axial	✗	1	35
RibFrac [57]	Lesion Seg.	Rib	Axial	✗	1	420
Adrenal ACC Ki67 [3]	Lesion Seg.	Adrenal Gland	Axial	✗	1	29
LNQ2023 [15]	Lesion Seg.	Lung	Axial	✗	1	393
NIH-LN [50]	Lesion Seg.	Lung	Axial	✗	1	175
CCC-18 [51]	Lesion Seg.	Chest & Abdomen	Axial	✗	✗	404
DeepLesion [55]	Lesion Det.	Whole Body	Axial	✗	✗	33K
TotalSegmentator [52]	Organ Seg.	Whole Body	Axial	✗	✗	1.2K
AbdomenAtlas [47]	Organ Seg.	Chest & Abdomen	Axial	✗	✗	8K
CTRATE [18]	Report Gen.	Chest	Axial	✓	✗	26K
BIMCV-R [10]	Report Gen.	Chest	Axial	✓	✗	8K
OminiAbnorm-CT-14K	Lesion Seg.		Axial	✓	340	10K
	Lesion Det.	Whole Body	Coronal	✓	255	2K
	Report Gen.		Sagittal	✓	223	1.6K

base QWen2.5-VL-7B model. As shown in Table 7, when we increase the input slices, there is no consistent performance improvement on any metric. We speculate this is mainly because multi-modal language models, which generally encode and project each input image into tokens independently, can hardly capture the subtle spatial relationships across adjacent slices. Therefore, we only take the center slice as image input to the multi-modal language model in the subsequent training and evaluation of OminiAbnorm-CT.

A.9 Ablation Study on Different Visual Prompts

Recent studies have revealed that VLMs exhibit varying perceptual capabilities for different forms of visual prompts [8]. Therefore, in the visual-prompted report generation task, we investigated the impact of different visual prompt formats to give insight on optimal design choices in application. Specifically, for each abnormality in our dataset, we simulated four distinct visual prompt types: center cropping, ellipse, contour, and bounding box, as input and evaluated OminiAbnorm-CT’s

Table 7: Impact of multi-slice context range on visual prompted report generation, with the base Qwen2.5-VL-7B model as baseline. Abbreviations: B = BLEU, RTSc = RaTEScore, BTSc = BERTScore, MTR = METEOR, R = Rouge, RG = RadGraph.

Input Slices	B-1	B-2	B-3	RTSc	BTSc	MTR	R-1	R-L	RG
<i>Axial (n=2193)</i>									
4 Adjacent Slices	9.39	2.98	0.45	31.12	83.52	14.90	11.51	9.01	2.46
2 Adjacent Slices	9.24	3.03	0.46	31.47	83.49	15.05	11.41	8.99	2.49
No Adjacent Slices	11.57	4.20	0.76	38.35	84.10	16.68	14.26	11.09	3.85
<i>Coronal (n=750)</i>									
4 Adjacent Slices	10.93	3.93	0.85	32.95	83.49	15.82	13.29	9.79	3.62
2 Adjacent Slices	10.89	3.85	0.73	33.06	83.48	15.87	13.34	9.85	3.71
No Adjacent Slices	13.62	3.54	0.66	37.26	84.19	13.49	14.97	11.47	3.37
<i>Sagittal (n=591)</i>									
4 Adjacent Slices	9.39	2.98	0.45	31.12	83.52	14.90	11.51	9.01	2.46
2 Adjacent Slices	11.48	4.16	0.94	33.86	83.32	15.70	13.64	9.97	3.75
No Adjacent Slices	13.28	3.54	0.63	35.67	83.98	13.01	14.75	11.34	2.91

generated reports respectively. We also take the maximum score among them for each abnormality, representing the theoretical best performance achievable by selecting the optimal visual prompt type for each specific abnormality, depending on its shape, location, and etc. As shown in Table 8, cropping the prompted area consistently underperforms across nearly all metrics (24 out of 27 total measurements), likely due to the loss of crucial contextual information outside the prompted region. The other individual visual prompting methods (ellipse, contour, and bounding box) demonstrate comparable performance. Notably, integrating multiple visual prompting techniques yields a substantial improvement across all metrics compared to the best individual prompt for each measure. This indicates significant performance variation when using different visual prompts for the same abnormality, suggesting that selecting appropriate prompt types based on abnormality morphology and location could be an effective strategy.

Table 8: Comparison of different visual prompt formats in visual prompted report generation task, with OminiAbnorm-CT fixed as baseline. Abbreviations: B = BLEU, RTSc = RaTEScore, BTSc = BERTScore, MTR = METEOR, R = Rouge, RG = RadGraph.

Prompt Type	B-1	B-2	B-3	RTSc	BTSc	MTR	R-1	R-L	RG
<i>Axial (n=2193)</i>									
Center Cropping	11.70	2.87	0.68	33.03	84.84	12.77	14.58	11.75	3.92
Ellipse	12.43	3.60	1.15	35.14	84.87	13.67	15.55	12.63	5.27
Contour	12.60	3.79	1.22	35.74	85.09	14.12	15.97	12.92	5.81
Bounding Box	12.35	3.69	1.26	35.46	84.92	13.65	15.76	12.80	5.63
Max	18.03	6.65	1.80	42.81	86.35	19.40	21.66	17.61	9.98
<i>Coronal (n=750)</i>									
Center Cropping	10.94	2.96	0.80	33.57	84.48	11.92	14.23	11.36	3.87
Ellipse	12.49	3.79	1.13	36.09	84.56	13.44	15.94	12.43	5.16
Contour	12.61	3.73	1.02	35.50	84.71	13.45	15.75	12.25	4.87
Bounding Box	12.15	3.70	1.12	35.12	84.38	13.27	15.68	12.13	4.68
Max	18.38	7.19	2.39	42.88	86.00	19.00	21.30	16.87	9.44
<i>Sagittal (n=591)</i>									
Center Cropping	10.98	2.73	0.39	32.23	84.20	11.98	14.45	11.01	3.05
Ellipse	11.37	3.10	0.65	34.36	84.01	12.19	14.45	10.95	3.46
Contour	11.08	2.95	0.57	34.19	84.22	12.01	14.38	11.10	3.22
Bounding Box	11.29	2.98	0.67	34.07	84.13	12.16	14.84	11.24	3.45
Max	17.29	6.48	1.82	41.77	85.62	17.45	20.43	15.87	7.51

A.10 Generation of Text Queries and Visual Prompts

We simulate four visual prompts for each annotated abnormality, mimicking how clinicians would select the most appropriate highlighting method based on the abnormality’s shape and location: (i) **cropped region**. We extract the minimum bounding box that completely contains the annotated lesion region, add a 50-pixel padding around this region, and crop the original image to center the abnormality; (ii) **ellipse**. We fit an optimal ellipse to the largest contour extracted from the lesion mask. (iii) **contour**. We smooth the lesion mask using Gaussian blur, detect its contours, and refine them with polygon approximation. (iv) **bounding box**. We identify the minimum bounding box that completely contains the annotated lesion region, and add a 10-pixel padding around.

To simulate radiologists approaching CT images with prior knowledge, we provide GPT-4o with patient information (complaints, medical history, etc) to generate text queries that inquire specific abnormality based on such preliminary information. We use the following prompt template:

Assuming a CT image has one or more abnormal findings, I will provide detailed information about them. Please help me generate prompts to test a VLM’s ability to localize and analyze specific abnormalities.

Requirements:

1. Generate prompts in English.
2. Ensure accurate information. The prompt content must stem from the real abnormality information, CT image reports, and doctor’s discussion results I provided. You may use equivalent expressions in medical terminology, but do not introduce any content beyond these provided information.
3. Clear indication. Ensure each prompt refers to the corresponding abnormality without confusion with other abnormalities in the image.
4. Clear task. Each prompt should end with a clear request for the VLM to perform localization and analysis tasks.
5. Simulate realistic pre-examination clinical queries. Create prompts that reflect how clinicians approach CT images with preliminary information (such as the patient’s complaints, medical history, other test results, etc., if available) and medical knowledge (such as common abnormalities associated with the patient’s information or typically found in this imaged region), without being overly specific. Importantly, prompts should be broad enough to guide examination of suspicious areas and must not include detailed descriptions or conclusions from findings, reports and discussion results that would only be available after examining the CT image, such as specific abnormality details, exact measurements, precise locations, or definitive characteristics that could only be determined after image interpretation.

Some appropriate examples:

\$Some Example Queries\$

6. Avoid data leakage. To evaluate the VLM’s ability to localize and analyze abnormalities independently, do not provide complete findings or diagnostic conclusions in the query. This prevents the VLM from bypassing the analytical process by retrieving answers directly from the prompt, while maintaining challenge authenticity.
7. Diversity. Generate at least 1 and at most 5 prompts with different perspectives for each abnormality. Each prompt should have clearly different focuses, avoiding content redundancy.

The information about all the abnormalities on the CT images:

\$Abnormal Findings\$

The clinical presentation of the patient corresponding to this CT image is:

\$Presentation\$

The overall report for the CT image containing these abnormalities is:

\$Whole Report\$

The doctors’ discussion results for the patient corresponding to this CT image are:

\$Impression\$

Your response must follow this exact format:

\$Output Template\$

A.11 Detailed Distribution of Abnormalities in OminiAbnorm-CT-14K



Figure 8: Distribution of OminiAbnorm-CT-14K across 82 anatomical structures and 40 major systems or organs. Darker blue indicates higher sample density. Abd. & Pelv. = Abdominal and Pelvic Cavity; Test., Epid., Scrot. = Testes, Epididymis, Scrotum; Morph. = Morphology; Pos. = Positional; Vent. & Subarach. = Ventricles and Subarachnoid.

Table 9: Detailed distribution of abnormality categories in OminiAbnorm-CT-14K.

Organ	Anatomical Structure	Category	Axial	Coronal	Sagittal
Brain	Cerebral parenchyma	Brain parenchymal atrophy	31	2	4
		Brain parenchymal edema	49	13	4
		Brain parenchymal soft tissue mass	280	57	57
		Brain parenchymal thin-walled cystic mass	52	1	3
		Brain parenchymal thick-walled cystic mass	17	0	1
		Brain parenchymal hemorrhage or contusion	198	42	31
		Acute infarct	88	1	0
		Lacunar infarct	54	11	8
		Encephalomalacia	27	6	3
		Brain parenchymal morphological alteration	102	31	23
		Other non-mass effect lesions	44	5	5
		Intracranial air	14	8	10
		Hyperdense lesions in brain parenchyma	72	24	44
		Others	35	13	6
	Ventricles and cisterns	Ventricular or cisternal enlargement	122	25	25
		Ventricular or cisternal soft tissue mass	49	8	6
		Ventricular or cisternal cystic mass	13	1	0
		Ventricular or cisternal hemorrhage	60	4	3
		Others	11	2	3
	Meninges (including dura mater, pia mater and arachnoid mater)	Meningeal cystic mass	4	0	0
		Meningeal soft tissue mass	8	9	6
		Meningeal hemorrhage	137	27	10
		Meningeal effusion	32	9	3
		Meningeal thickening	6	0	0
		Others	4	0	2
	Pituitary and Sellar Region	Pituitary stalk thickening	0	0	0
		Pituitary stalk lateral displacement	0	0	0
		Pituitary enlargement	0	0	2
		Pituitary atrophy	0	2	4
		Pituitary calcification	0	0	3
		Pituitary or sella region soft tissue mass	20	16	27
		Pituitary or sella region cystic mass	3	5	6
		Others	1	0	0
Spine	Spinal Cord	Spinal cord compression	3	0	2
		Spinal cord soft tissue mass	12	1	6
		Spinal cord hemorrhage or contusion	0	0	0
		Spinal morphological alteration	0	0	0
		Syringomyelia	0	0	0
		Others	4	0	1
	Intervertebral disc	Intervertebral disc morphological alteration	4	2	1
		Intervertebral disc ossification or calcification	0	0	0
		Intervertebral disc gas	4	3	2
		Intervertebral disc extrusion	0	0	0
		Intervertebral disc soft tissue mass	5	1	1
		Others	0	0	1
	Spinal meninge (including dura mater, arachnoid mater, and pia mater)	Spinal meningeal hemorrhage	0	0	0
		Spinal meningeal effusion	0	0	1
		Spinal meningeal thickening	0	0	0
		Meningeal soft tissue mass	7	2	6
		Meningeal cystic mass	0	2	0
		Others	2	1	5

Table 10: (Continued) Detailed distribution of abnormality categories in OminiAbnorm-CT-14K.

Organ	Anatomical Structure	Category	Axial	Coronal	Sagittal
Eye	Eyeball	Eyeball atrophy	4	1	2
		Eyeball positioning or morphological alteration	44	7	6
		Eyeball density alteration	45	20	14
		Eyeball soft tissue mass	19	3	1
		Eyeball wall thickening	5	3	0
		morphological alteration			
		Complete or partial absence of eyeball structure	2	0	0
		Others	2	2	0
	Ocular Adnexa	Orbital density changes	54	36	15
		Intraorbital gas	4	4	3
		(e.g., soft tissue mass, fluid accumulation)			
		Extraocular muscle hypertrophy or atrophy	16	43	11
		Optic nerve thickening or soft tissue mass	7	3	7
		Optic nerve atrophy	0	0	0
		Others	3	2	3
	Lacrimal gland and lacrimal sac	Lacrimal gland and lacrimal sac enlargement or mass	19	12	5
		Lacrimal gland and lacrimal sac calcification or fluid	4	2	0
		Others	1	0	1
Ear	External Ear	External auditory canal stenosis or atresia	5	1	2
		External auditory canal soft tissue mass	11	5	1
		Others	1	1	0
	Middle Ear	Middle ear fluid or hemorrhage	5	0	0
		Middle ear soft tissue mass	23	23	3
		Ossicular chain destruction or deformity	7	2	0
		Tympanic membrane thickening or calcification	2	2	0
		Middle ear gas density change	6	0	1
		Others	1	2	0
	Inner Ear	Inner ear congenital structural alteration	2	1	0
		Inner ear bone destruction or sclerosis	11	4	0
		Internal auditory canal enlargement or narrowing	2	0	0
		Labyrinthine structural alteration	4	2	0
		Others	1	1	0
Sinus	Sinus cavity	Sinus effusion	18	8	0
		Sinus hemorrhage	6	3	3
		Sinus soft tissue mass	98	85	33
		Sinus cystic mass	8	5	1
		Sinus mucosal thickening	24	25	7
		Others	9	3	2
	Sinus ostium	Sinus obstruction or stenosis	1	4	0
		Sinus widening	0	0	1
		Others	1	1	0
	Nasal septum	Nasal septum deviation or thickening	7	6	0
		Nasal septum perforation or defect	1	1	0
		Others	6	2	0

Table 11: (Continued) Detailed distribution of abnormality categories in OminiAbnorm-CT-14K.

Organ	Anatomical Structure	Category	Axial	Coronal	Sagittal
Pharynx	Pharynx (including nasopharynx, oropharynx, and hypopharynx)	Pharyngeal narrowing or obstruction	4	2	1
		Pharyngeal soft tissue mass	46	14	10
		Pharyngeal cystic mass	10	2	4
		Pharyngeal wall thickening	4	3	0
		Pharyngeal foreign body	0	0	0
		Others	3	4	1
	Larynx	Laryngeal narrowing or obstruction	3	2	0
		Vocal cord asymmetry	2	0	0
		Vocal cord soft tissue mass	6	1	1
		Laryngeal cartilage calcification	0	0	0
		Laryngeal cystic mass	1	1	0
		Laryngeal foreign body	1	0	0
		Others	1	0	0
	Pharyngeal space	Pharyngeal space soft tissue mass	46	23	16
		Pharyngeal space cystic mass	13	6	2
		Pharyngeal emphysema	7	0	0
		Others	5	7	1
Parotid gland	Parotid gland	Parotid gland enlargement	20	2	0
		Parotid gland atrophy	4	0	0
		Parotid gland soft tissue mass	33	2	2
		Parotid gland cystic mass	16	0	0
		Parotid gland calcification or stone	15	0	2
		Others	10	0	0
Thyroid gland	Thyroid gland	Thyroid enlargement	12	2	2
		Thyroid atrophy	1	0	0
		Thyroid soft tissue mass	41	4	0
		Thyroid cystic mass	3	1	0
		Thyroid calcification	1	0	0
		Ectopic thyroid gland	5	1	0
		Others	6	0	1
Trachea	Tracheal lumen	Tracheal stenosis or obstruction	12	4	7
		Tracheal dilatation	11	5	2
		Tracheal soft tissue mass	12	6	1
		Tracheal wall thickening	9	0	0
		Tracheal wall calcification	3	1	4
		Tracheal wall defect	3	0	2
		Others	1	0	2
Lung	pulmonary parenchyma	Atelectasis	106	10	3
		Incomplete lung expansion	52	3	1
		Pulmonary consolidation	203	24	2
		Pulmonary ground-glass opacities	343	52	5
		Pulmonary emphysema	45	10	2
		Pulmonary solitary nodule or mass	226	46	10
		Pulmonary diffusely distributed multiple nodules	285	76	3
		Pulmonary parenchymal fibrosis	42	12	0
		Pulmonary thin-walled cavitation	48	6	1
		Pulmonary thick-walled cavities	44	1	0
		Pulmonary cystic mass	53	14	1
		Others	14	6	1
	Bronchi	Bronchiectasis	97	19	6
		Bronchial wall thickening, stenosis, or occlusion	15	11	5
		Bronchial foreign body	4	1	0
		Others	3	0	1

Table 12: (Continued) Detailed distribution of abnormality categories in OminiAbnorm-CT-14K.

Organ	Anatomical Structure	Category	Axial	Coronal	Sagittal
Lung	Lung interstitial	Lung interstitial fibrosis and thickening	78	10	0
		Honeycomb lung	34	0	0
		Others	2	0	0
	Pleura	Pleural thickening	39	10	1
		Pleural effusion	268	27	3
		Pneumothorax	36	2	0
		Pleural calcification	24	0	1
		Pleural soft tissue mass	50	8	0
		Others	8	1	1
Mediastinum	Mediastinal soft tissue	Mediastinal shift	29	4	0
		Mediastinal soft tissue mass	200	31	15
		Mediastinal cystic mass	19	0	2
		Mediastinal hemorrhage	15	0	0
		Mediastinal emphysema	58	7	1
		Others	10	0	0
Diaphragm	Diaphragm	Diaphragmatic hernia	19	16	12
		Diaphragmatic elevation	5	4	0
		Diaphragmatic soft tissue mass	7	2	0
		Others	0	2	0
Thymus	Thymic parenchyma	Thymic enlargement	1	0	0
		Thymic atrophy	0	0	0
		Thymic soft tissue mass	6	0	0
		Thymic cystic mass	0	0	0
		Thymic calcification	4	0	0
		Others	1	0	0
Oral cavity	Oral Soft Tissue	Oral soft tissue mass	8	0	0
		Oral cystic mass	3	0	0
		Oral soft tissue calcification	0	0	0
		Others	0	0	0
	Teeth and alveolar bone	Dental developmental anomalies	1	0	0
		Dental positional anomalies	3	4	5
		Dental calcification or caries	3	0	0
		Alveolar bone resorption or hyperplasia	3	0	0
		Alveolar soft tissue mass	8	2	0
		Alveolar cystic mass	8	1	1
		Others	0	1	0
	Cardiac chambers (atrium or ventricle)	Cardiac chamber enlargement	41	7	3
		Cardiac chamber mass	28	7	2
		Others	17	1	0
Heart	Myocardium	Myocardial hypertrophy	4	1	1
		Myocardial thinning	3	0	0
		Myocardial calcification	4	1	0
		Myocardial density alteration	6	0	0
		Others	3	3	0
	Heart valve	Valvular calcification	3	0	0
		Others	3	0	0
	Pericardium	Pericardial thickening	9	0	2
		Pericardial calcification	6	1	0
		Pericardial effusion	54	7	2
		Pericardial hemorrhage	2	0	0
		Pericardial emphysema	6	1	0
		Others	4	0	0

Table 13: (Continued) Detailed distribution of abnormality categories in OminiAbnorm-CT-14K.

Organ	Anatomical Structure	Category	Axial	Coronal	Sagittal
Heart	Coronary arteries	Coronary artery myocardial bridge	1	0	0
		Coronary artery dilation	0	0	0
		Others	3	1	0
Vascular structure	Artery	Arterial widening	66	24	9
		Aneurysm	138	44	39
		Atherosclerotic plaque of arterial wall	39	13	4
		Arterial wall ulcer	8	2	2
		Arterial dissection or intramural hematoma	22	15	8
		Arterial stenosis	24	8	10
		Arterial occlusion	55	9	0
		Arterial filling defect	80	23	8
		Arterial contour abnormality	51	23	23
		Arteriovenous fistula	16	7	1
		Arterial wall inflammatory exudate	4	0	0
		Others	39	9	7
	Vein	Venous dilation	41	4	6
		Varicosity	23	11	9
		Venous wall inflammation	0	0	0
		Venous stenosis	7	1	1
		Venous occlusion	5	2	1
		Venous filling defect	48	12	3
		Venous morphological abnormality	29	6	3
		Venous wall inflammatory exudate	2	1	0
		Others	13	8	0
	Capillary	Capillary dilation	0	0	0
		Capillary malformation proliferation	1	0	0
		Others	0	0	0
Gastrointestinal tract (including esophagus, stomach, and intestines)	Gastrointestinal lumen	Gastrointestinal dilatation	265	212	112
		Gastrointestinal narrowing	20	5	6
		Gastrointestinal foreign body	2	6	0
		Gastrointestinal air-fluid level	31	8	5
		Gastrointestinal luminal contents abnormal density	17	6	4
		Others	8	3	1
	Gastrointestinal tract wall	Gastrointestinal wall thickening	398	212	120
		Gastrointestinal wall mass	103	56	26
		Gastrointestinal wall rupture and perforation	43	12	4
		Gastrointestinal wall ulceration	0	0	0
		Others	7	9	5
	Gastrointestinal positioning abnormality	Gastrointestinal herniation or deformity	117	67	30
		Others	5	1	1
	Gastrointestinal morphological abnormalities	Gastrointestinal diverticulum	53	35	15
		Gastrointestinal malrotation and volvulus	17	17	3
		Gastrointestinal annular or concentric abnormality	28	22	10
		Others	2	1	2
	Mesentery	Mesenteric volvulus	3	4	2
		Mesenteric edema	10	3	3
		Mesenteric panniculitis	26	6	6
		Mesenteric soft tissue mass	28	6	9
		Others	0	4	2

Table 14: (Continued) Detailed distribution of abnormality categories in OminiAbnorm-CT-14K.

Organ	Anatomical Structure	Category	Axial	Coronal	Sagittal
Liver	Hepatic parenchyma	Hepatic parenchymal morphological alteration	99	34	11
		Hepatic parenchymal hyperdensity	18	2	0
		Hepatic parenchymal hypodensity	71	25	9
		Hepatic parenchymal soft tissue mass	439	58	20
		Hepatic parenchymal thin-walled cystic mass	124	23	10
		Hepatic parenchymal thick-walled cystic mass	21	6	4
		Liver contusion or hemorrhage	10	3	0
		Intrahepatic bile duct emphysema	13	1	0
		Intrahepatic bile duct fluid accumulation	0	0	0
		Intrahepatic biliary stones or calcification	7	0	0
		Others	16	4	1
Gallbladder	Gallbladder lumen	Gallbladder distension	39	10	1
		Gallbladder atrophy or shrinkage	4	1	0
		Gallbladder stone	87	22	2
		Gallbladder contents density change	32	5	0
		Others	3	1	0
	Gallbladder wall	Gallbladder wall thickening	53	11	1
		Gallbladder wall calcification	9	1	0
		Gallbladder wall mass	16	2	1
		Gallbladder wall rupture	11	1	0
		Others	3	1	1
	Gallbladder morphology	Gallbladder position alteration	1	0	0
		Gallbladder congenital morphological variation	0	0	0
		Others	1	1	0
	Extrahepatic bile ducts	Extrahepatic bile duct dilation	26	8	0
		Extrahepatic bile duct wall thickening	2	0	0
		Extrahepatic bile duct soft tissue mass	1	0	1
		Extrahepatic bile duct cystic mass	1	1	0
		Extrahepatic bile duct stenosis or obstruction	2	0	0
		Extrahepatic bile duct content density alteration	6	1	0
		Extrahepatic bile duct stone	15	5	0
		Extrahepatic bile duct injury or rupture	0	0	0
		Others	1	0	0
Pancreas	Pancreatic parenchyma	Pancreatic parenchymal soft tissue mass	137	8	4
		Pancreatic cystic mass	69	7	4
		Pancreatic calcification	20	1	0
		Pancreatic enlargement	60	1	1
		Pancreatic atrophy	8	1	1
		Others	16	0	0
	Pancreatic duct	Pancreatic ductal dilatation	13	3	0
		Pancreatic ductal stone	3	0	0
		Others	0	0	0
	Pancreatic morphology	Pancreatic congenital anomaly	5	0	0
		Pancreatic positional displacement	1	0	0
		Others	1	0	0
Spleen	Splenic parenchyma	Splenic parenchymal calcification	15	0	1
		Splenic parenchymal soft tissue mass	52	11	3
		Splenic parenchymal cystic mass	27	10	0
		Splenic parenchymal infarct	19	1	0
		Splenic parenchymal rupture	12	1	0
		Others	18	2	0
	Spleen morphology	Spleen enlargement	102	22	5
		Others	17	1	0

Table 15: (Continued) Detailed distribution of abnormality categories in OminiAbnorm-CT-14K.

Organ	Anatomical Structure	Category	Axial	Coronal	Sagittal
Abdominopelvic peritoneum	Abdominopelvic peritoneum	Peritoneal inflammatory exudate	75	19	10
		Peritoneal thickening	19	3	1
		Peritoneal calcification	5	1	0
		Peritoneal soft tissue mass	364	135	90
		Peritoneal cystic mass	102	34	22
		Abdominopelvic fluid	280	96	43
		Abdominopelvic hemorrhage	68	3	1
		Abdominopelvic free air	61	17	10
		Retroperitoneal fibrosis	1	0	0
		Peritoneal or retroperitoneal lymph enlargement	17	18	4
		Extravasation of gastrointestinal content	0	1	0
		Abdominopelvic contrast agent leakage	22	13	4
		Others	12	12	2
Kidney	Renal Parenchyma	Renal parenchymal soft tissue mass	150	81	29
		Renal parenchymal cystic mass	239	68	21
		Renal parenchymal calcification	9	9	2
		Renal parenchymal or subcapsular hemorrhage	11	3	2
		Renal infarct	8	3	0
		Others	27	8	1
	Renal pelvis and ureter	Hydronephrosis	81	63	3
		Ureteral dilatation	35	29	4
		Ureteral stricture or obstruction	1	1	0
		Ureteric stone	59	60	19
		Double renal pelvis and/or double ureter anomaly	5	3	1
		Renal pelvis soft tissue mass	13	4	0
		Renal pelvic cystic mass	1	3	0
		Others	4	5	2
	Renal morphology and position abnormalities	Renal morphological anomaly	33	20	1
		Renal enlargement	56	16	1
		Renal atrophy	23	6	2
		Ectopic or transplanted kidney	17	13	5
		Others	3	2	0
Bladder	Bladder cavity	Bladder distention	4	0	1
		Bladder stone	24	5	3
		Bladder content density change	13	2	1
		Others	4	3	0
	Bladder wall	Bladder wall diffuse thickening	17	5	6
		Bladder wall calcification	1	3	1
		Bladder wall focal thickening or soft tissue mass	69	7	3
		Bladder wall defect or fistula	4	0	1
		Bladder wall emphysema	9	0	1
		Bladder wall diverticulum	31	2	2
		Others	1	0	0
	Bladder morphology	Bladder position displacement	9	2	2
		Bladder morphological anomaly	2	0	0
		Others	1	0	2

Table 16: (Continued) Detailed distribution of abnormality categories in OminiAbnorm-CT-14K.

Organ	Anatomical Structure	Category	Axial	Coronal	Sagittal
Adrenal gland	Adrenal gland	Adrenal soft tissue mass	122	17	1
		Adrenal cystic mass	32	0	0
		Adrenal calcification	0	3	0
		Adrenal gland thickening	16	0	0
		Adrenal atrophy	0	0	0
		Others	15	0	0
Prostate	Prostate	Prostate enlargement	18	12	14
		Prostate atrophy	0	0	0
		Prostatic cystic mass	2	0	0
		Prostatic soft tissue density anomaly	2	0	1
		Prostatic calcification	2	1	2
		Prostatic hemorrhage	0	0	0
		Others	0	0	0
Seminal vesicle	Seminal vesicle	Seminal vesicle soft tissue mass	1	0	0
		Seminal vesicle calcification	0	0	1
		Seminal vesicle cystic mass	3	0	0
		Others	0	0	0
Testes, epididymis, and scrotum	Testis	Testicular enlargement	1	0	0
		Testicular atrophy	0	0	0
		Testicular soft tissue mass	1	0	0
		Testicular calcification	0	0	0
		Testicular cystic mass	0	0	0
		Testicular torsion	0	0	0
		Testicular hemorrhage and rupture	0	0	0
		Others	0	0	0
	Scrotum	Scrotal effusion	1	0	0
		Scrotal hematoma	0	0	0
		Scrotal soft tissue mass	1	0	0
		Scrotal wall thickening	0	0	0
		Others	2	0	0
	Epididymis	Epididymis enlargement	0	0	0
		Epididymal soft tissue mass	0	0	0
		Epididymal calcification	0	0	0
		Epididymal cystic mass	0	0	0
		Epididymal thickening	0	0	0
		Others	0	0	0
Penis	Penis	Penile morphological anomaly	0	0	0
		Penile soft tissue mass	0	0	0
		Penile calcification	0	0	0
		Urethral calculi or foreign body	6	2	1
		Urethral Stricture	0	0	0
		Urethral dilation	1	0	0
		Others	4	0	0
Uterus	Uterus	Uterine morphological anomaly	7	1	2
		Uterine enlargement	15	3	6
		Uterine soft tissue mass	50	4	7
		Uterine calcification	7	0	2
		Uterine cavity effusion	2	0	1
		Uterine cavity hemorrhage	2	0	0
		Uterine cystic mass	4	0	0
		Others	4	1	1

Table 17: (Continued) Detailed distribution of abnormality categories in OminiAbnorm-CT-14K.

Organ	Anatomical Structure	Category	Axial	Coronal	Sagittal
Fallopian tube	Fallopian tube	Fallopian tube thickening	3	0	0
		Fallopian tube cystic mass	2	0	1
		Fallopian tube soft tissue mass	12	4	2
		Fallopian tube effusion	2	0	0
		Fallopian tube hemorrhage	0	0	0
		Fallopian tube calcification	0	0	0
		Others	0	0	0
Ovary	Ovary	Ovarian enlargement	9	3	0
		Ovarian Atrophy	0	0	0
		Ovarian cystic mass	85	12	6
		Ovarian soft tissue mass	96	6	3
		Ovarian calcification	3	1	0
		Ovarian torsion	9	0	0
		Others	1	1	0
Vagina and vulva	Vagina and vulva	Vaginal soft tissue mass	0	0	0
		Vaginal cystic mass	9	0	0
		Vaginal hemorrhage	1	0	0
		Vaginal emphysema	3	0	4
		Vaginal anatomical anomaly	3	0	1
		Others	6	0	0
Breast	Breast gland	Breast gland enlargement	2	0	0
		Breast gland atrophy	0	0	0
		Breast gland soft tissue mass	36	9	2
		Breast gland calcification	0	0	0
		Breast gland cystic mass	0	0	0
		Others	6	0	0
	Breast duct	Breast duct dilation	0	0	0
		Breast duct calcification	0	0	0
		Others	0	0	0
	Nipple	Nipple retraction	0	0	0
		Nipple calcification	0	0	0
		Others	0	0	0
	Areola	Areola thickening	1	0	0
		Others	0	0	0
Skeletal system	Skeletal system	Osteoporosis	9	1	8
		Osteomalacia	2	0	1
		Bone destruction or soft tissue mass	219	124	117
		Bone cystic mass	19	32	17
		Osseous sclerosis	179	80	121
		Osteonecrosis	64	13	24
		Bone fracture	308	172	247
		Periosteal reaction	23	9	5
		Periosteal thickening	8	5	1
		Bone callus and post-fracture healing	10	8	2
		Scar of fracture fixation removal	0	0	0
		Bone deformation	67	44	73
		Skeletal asymmetry	10	2	1
		Cartilage calcification	4	4	8
		Chondral calcification	5	0	1
		Others	30	50	26

Table 18: (Continued) Detailed distribution of abnormality categories in OminiAbnorm-CT-14K.

Organ	Anatomical Structure	Category	Axial	Coronal	Sagittal
Joint	Joint	Joint space narrowing	6	12	3
		Joint space widening	3	0	3
		Joint cartilage degradation	1	0	2
		Joint cartilage calcification	3	1	1
		Joint capsule thickening	0	0	0
		Intra-articular effusion	13	3	2
		Intra-articular hemorrhage	4	0	0
		Intra-articular gas	1	0	4
		Joint periarticular soft tissue swelling	2	0	0
		Irregular articular surfaces	12	5	2
		Joint subluxation or dislocation	30	14	22
		Intra-articular loose body	8	1	2
		Others	5	12	2
Muscle	Muscle	Muscle swelling	8	5	1
		Muscle atrophy	13	1	0
		Muscular soft tissue mass	40	9	2
		Muscular cystic mass	11	13	3
		Muscular hemorrhage	7	0	1
		Muscle calcification	3	0	0
		Muscle open injury and tear	0	0	0
		Tendon calcification	19	3	13
		Tendon tear or rupture	1	0	1
		Others	7	4	1
Skin and subcutaneous fat	Skin and subcutaneous fat	Subcutaneous soft tissue mass	141	47	28
		Subcutaneous edema	18	6	2
		Subcutaneous effusion	26	3	1
		Subcutaneous inflammatory exudate	10	2	1
		Subcutaneous swelling	60	10	15
		Subcutaneous open wound and laceration	15	5	2
		Subcutaneous calcification	12	0	0
		Subcutaneous fat necrosis	2	0	0
		Abdominal wall hernia	48	3	6
		Others	33	5	9
Agenesis or ectopia	Agenesis or ectopia	Congenital developmental anomaly	78	35	14
		Postoperative changes	42	16	5
		Situs inversus	10	7	1
		Others	2	0	0
Implantation of artificial object	Implantation of artificial object	Implantation of artificial object	179	91	53
		Others	17	3	8